arXiv:1608.00934v1 [astro-ph.SR] 2 Aug 2016

SEMI-EMPIRICAL MODELING OF THE PHOTOSPHERE, CHROMOSPHERE, TRANSITION REGION, AND CORONA OF THE M-DWARF HOST STAR GJ 832[1]

J.M. Fontenla[2], Jeffrey L. Linsky[3], Jesse Witbrod[4], Kevin France[5], A. Buccino[6,7], Pablo Mauas[6], Mariela Vieytes[6], and Lucianne M. Walkowicz[8]

Received _____; accepted _____

To be submitted to ApJ

[2]NorthWest Research Associates, Boulder, CO 80301; johnf@digidyna.com

[4]University of Colorado Boulder, CO 80301; jesse.witbrod@colorado.edu

[3]JILA, University of Colorado and NIST, Boulder, CO 80309-0440; jlinsky@jila.colorado.edu

[4]University of Colorado Boulder, CO 80301; jesse.witbrod@colorado.edu

[5]LASP, University of Colorado Boulder, CO 80309-0600; kevin.france@lasp.colorado.edu

[6]Instituto de Astronomía y Física del Espacio (CONICET-UBA), C.C. 67, Sucursal 28, C1428EHA, Buenos Aires, Argentina; abuccino@iafe.uba.ar, pablo@iafe.uba.ar, mariela@iafe.uba.ar

[7]Visiting Astronomer, Complejo Astronómico El Leoncito operated under agreement between the Consejo Nacional de Investigaciones Científicas y Técnicas de la República Argentina and the National Universities of La Plata, Córdoba and San Juan.

[8]The Adler Planetarium, Chicago, IL 60605; LWalkowicz@adlerplanetarium.org

ABSTRACT

Stellar radiation from X-rays to the visible provides the energy that controls the photochemistry and mass loss from exoplanet atmospheres. The important extreme ultraviolet (EUV) region (10–91.2 nm) is inaccessible and should be computed from a reliable stellar model. It is essential to understand the formation regions and physical processes responsible for the various stellar emission features in order to predict how the spectral energy distribution varies with age and activity levels. We compute a state-of-the-art semi-empirical atmospheric model and the emergent high-resolution synthetic spectrum of the moderately active M2 V star GJ 832 as the first of a series of models for stars with different activity levels. Using non-LTE radiative transfer techniques and including many molecular lines, we construct a one-dimensional simple model for the physical structure of the star's chromosphere, chromosphere-corona transition region, and corona. The synthesized spectrum for this model fits the continuum and lines across the UV to optical spectrum. Particular emphasis is given to the emission lines at wavelengths shorter than 300 nm observed with *HST*, which have important effects on the photochemistry in the exoplanet atmospheres. The FUV line ratios indicate that the transition region of GJ 832 is more biased to hotter material than that of the quiet Sun. The excellent agreement of our computed EUV luminosity with that obtained by two other techniques indicates that our model predicts reliable EUV emission from GJ 832. We find that unobserved EUV flux of GJ 832, which heats the outer atmospheres of exoplanets and drives their mass loss, is comparable to the active Sun.

Subject headings: stellar atmospheres — stellar chromospheres — ultraviolet spectra — stars: individual(GJ 832)

1. INTRODUCTION AND MOTIVATION

The discovery of large numbers of exoplanets by the *Kepler* (Koch et al. 2010) and *CoRoT* (Baglin 2003) satellites and by ground-based radial velocity surveys has stimulated enormous interest in determining the properties and radiative output of M dwarf host stars. The low mass and luminosity of M dwarfs makes these stars favorable targets for the discovery and characterization of exoplanets in their habitable zones (e.g., Kasting, Whitmire, & Reynolds 1993; Scalo et al. 2007; Tarter et al. 2007; Kopparapu et al. 2013). These exoplanets are potentially easier to discover because they have large orbital radial velocities and relatively high probabilities for transits as a consequence of their being much closer to their host stars than for solar-type stars. Because M dwarf stars are much smaller and cooler than solar-type stars, their exoplanets occult a larger fraction of the stellar surface during transits with higher contrast between the exoplanet's faint absorption and emission spectra and the star's emission. Unfortunately, variability of the stellar UV and optical flux due to rotation and starspots complicates the analysis of transit light curves for exoplanets of M dwarf stars (e.g., Llama & Shkolnik 2015) and even the detection of habitable-zone exoplanets (Newton et al. 2016a).

Dressing & Charbonneau (2015) extracted from the *Kepler* data the mean number of Earth-size (0.5–1.4 R_E) exoplanets with orbital periods shorter than 50 days, corresponding to orbital distances that place many exoplanets inside the habitable zones of M dwarfs. They found that the occurrence rate of such planets is $0.16^{+0.17}_{-0.07}$ per cool dwarf and predicted with 95% confidence that the nearest nontransiting Earth-sized planet in its habitable zone

[1]Based on observations made with the NASA/ESA Hubble Space Telescope obtained from the Data Archive at the Space Telescope Science Institute, which is operated by the Association of Universities for Research in Astronomy, Inc., under NASA contract NAS AR-09525.01A. These observations are associated with programs #12034, 12035, 12464.

is located within 5 pc of the Sun. Kopparapu et al. (2013) proposed that the occurrence rate for such planets is about a factor of three larger based on new calculations of the habitable zone boundaries, which will place the likely location of the nearest habitable planet even closer than 5 pc. These predictions are powerful arguments for studying M-dwarf stars, the closest and most numerous stars in the Galaxy, whether or not they are presently known to harbor exoplanets. The upcoming *Transiting Exoplanet Survey Satellite (TESS)* and the *James Webb Space Telescope (JWST)* missions will play major roles in these studies.

The many observational studies of the optical Hα and Ca II H and K lines (e.g., Stauffer & Hartmann 1986; Robinson, Cram, & Giampapa 1990; Houdebine & Stempels 1997; Mauas 2000; Walkowicz & Hawley 2009; Pérez Martínez, Schröder, and Hauschildt 2014) have until now provided the principle diagnostics for modeling the magnetically heated gas in the chromospheres of low-mass stars. The presence and strength of Hα emission is the commonly used indicator of activity levels in M stars and even brown dwarfs (Berger et al. 2010). While the cores of the Ca II lines increase monotonically with magnetic heating and provide an unambiguous measure of stellar activity, the Hα line behaves differently with increasing activity. Cram & Giampapa (1987), Houdebine & Stempels (1997), and later modelers have predicted that with increasing chromospheric heating the Hα absorption line, which is very weak in the least active cool stars, first becomes a deeper absorption line and then fills-in to become an emission line. An accurate measure of the correlation of the fluxes or equivalent widths of the Hα and Ca II lines requires simultaneous observations of the Ca II and Hα lines, especially for the highly variable M dwarfs. Walkowicz & Hawley (2009) obtained simultaneous high-resolution spectra of the Ca II and Hα lines in M3 V stars. They observed a strong positive correlation of Hα and Ca II emission in active stars but only a weak or nonexistent correlation for inactive and moderately active stars, because for a large range of Ca II equivalent widths there is only a very small range of in Hα equivalent widths. This uncertain correlation for low activity

stars, which has been noted by previous observers, (e.g., Robinson, Cram, & Giampapa 1990; Buccino et al. 2011, 2014)), highlights the need for spectral diagnostics of emission features that all have a monotonic dependence on activity and thus should be positively correlated. An example is the correlation of the chromospheric Mg II emission lines (similar to the Ca II emission lines) with X-ray emission for M stars as found by Stelzer et al. (2013) and others.

X-ray observations of M-dwarf coronae show a nearly four orders-of- magnitude range in X-ray luminosity (L_X) between the least and most active M dwarfs and a correlation of L_X with X-ray spectral hardness and thus with higher coronal temperatures (Schmitt, Fleming, & Giampapa 1995; Fleming, Schmitt, & Giampapa 1995). Sanz-Forcada et al. (2011) has computed the total X-ray and extreme-ultraviolet flux for many stars, including GJ 832, from their observed X-ray spectra and developed scaling laws for this flux as a function of stellar age. During flares, M dwarfs show both enhanced X-ray emission and hotter coronal plasma (Robrade & Schmitt 2005). Searches for effects of exoplanets on the chromospheres and coronae of their host stars have provided some evidence for stellar-planetary interactions (Shkolnik, Walker, and Bohlender 2003; Lanza 2008; Shkolnik et al. 2005; Kashyap, Drake, & Saar 2008; Poppenhaeger, Robrade, & Schmitt 2010; Poppenhaeger & Wolk 2014). Very recently, France et al. (2016) found that additional heating in host star's chromosphere-corona transition regions (hereafter called transition regions) is correlated with the presence of a close-in exoplanet.

High-resolution ultraviolet (UV) spectroscopy provides a wide range of diagnostics for computing semiempirical models of M dwarfs from the top of the photosphere through the chromosphere and into the corona. An excellent example of such a spectrum is the spectral atlas of the young dM1e star AU Mic obtained with the E140M grating (resolution $\lambda/\Delta\lambda = 45,000$) of the Space Telescope Imaging Spectrograph (STIS) on the *Hubble*

Space Telescope (HST). In this spectrum covering the wavelength region 117.5–170 nm, Pagano et al. (2000) identified 142 emission lines of 28 species extending from chromospheric neutrals (e.g., C I and O I) and ions (Fe II and Si II), through ions formed in the transition region between 20,000 K and 200,000 K (C II–IV, Si III–IV, O III–V, and N V), and into the corona (Fe XXI 135.4 nm line formed at 10^7 K). With this rich group of emission lines, Pagano et al. (2000) were able to construct an emission-measure distribution for the stellar chromosphere and transition region and to compute the electron density in the transition region from O IV intersystem line ratios.

The MUSCLES (Measurements of the Uv Spectral Characteristics of Low Mass Exoplanetary Systems) observing program (France et al. 2013) used both STIS and the Cosmic Origins Spectrograph (COS) on *HST* to obtain 115–314 nm spectra of six weakly active M dwarfs hosting exoplanets, including GJ 832. These spectra have resolutions of 7.5–17 km s^{-1} in the 115–179.5 nm region and 2.6 km s^{-1} in the near UV (NUV, 170–300 nm) including the Mg II h and k lines near 280 nm. An important result of this program is that while the NUV spectra of M dwarfs are a factor of 10^3 times fainter than the Sun at the habitable zone distance from the star, the far-UV (FUV, 115–170 nm) spectra formed in the chromospheres of M dwarfs have fluxes comparable to or brighter than the Sun (France et al. 2012). The reconstructed Lyman-alpha (Ly-α) emission line corrected for interstellar absorption in M dwarf spectra has flux comparable to the entire rest of the 116–305 nm spectrum (France et al. 2013). Fluxes for these stars, including the reconstructed Ly-α flux, are included in the MAST website.[2]

The MUSCLES Treasury Survey extends the previous MUSCLES pilot observing program to include quasi-simultaneous X-ray through near-IR observations of 7 M and 4 K dwarf host stars located within 20 pc of the Sun. France et al. (2016) present an

[2]https://archive.stsci.edu/prepds/muscles/

overview of the survey showing examples of the spectra and spectral energy distributions (SEDs) between 0.5 nm and 5.5μm. Youngblood et al. (2016) compute reconstructions of the Lyman-α lines and use the reconstructed Lyman-α fluxes to estimate the unobservable extreme ultraviolet fluxes (EUV, 10-91.2 nm) of the 11 stars. In the third of the initial survey papers, Loyd et al. (2016) describe the stitching together of the different data sets that constitute the spectral energy distributions (SEDs) and compute photodissociation spectra of different molecules given the unattenuated SEDs of three host stars.

The observed UV spectra of M dwarfs are essential input for the computation of photochemical models of exoplanet atmospheres. The NUV stellar flux dissociates O_2, O_3, and other molecules, while the FUV flux dissociates H_2O, CO_2, CH_4, and other molecules. The stellar particle flux during a large flare can even deplete much of a planetary atmosphere's ozone (Segura et al. 2010). The very bright Ly-α line plays a major role in the photochemical processes. For example, photochemical models for the mini-Neptune GJ 436b (Miguel et al. 2015), using the MUSCLES data as input, show that the flux of Ly-α and other lines in the stellar FUV spectrum photodissociate H_2O, CO_2, and CH_4 in the 10^{-4} bar (10 N m^{-2}) and higher layers, producing atomic hydrogen and oxygen. EUV radiation below 91.2 nm ionizes hydrogen that then heats and inflates the outer atmospheres of close-in exoplanets (e.g., Murray-Clay, Chiang, and Murray 2009; Chadney et al. 2015). This is important for the evolution of planetary atmospheres, because hydrogen is readily lost through hydrodynamic outflow and ion pickup by the magnetic stellar wind in distended atmospheres. This process may also explain the loss of the Martian atmosphere (Brain et al. 2010). Whether or not an exoplanet in the habitable zone can support life forms depends crucially on the stability and chemical composition of its atmosphere.

The objective of this paper is to create the first complete physical model of a representative M dwarf, extending from its photosphere to its corona, that matches the

observed spectrum and can predict the unobserved portions of the stellar spectrum. Because the physical mechanisms that heat the chromospheres and coronae of late-type stars are not well understood, we use spectra over a broad range of wavelengths to test semi-empirical thermal structures of stellar chromospheres and coronae. By computing a physically consistent semi-empirical model, we can determine where in the atmosphere each spectral line and continuum is formed and note differences between where these features are formed in M dwarf models compared to solar models. Based on a realistic atmospheric model describing these formation temperatures and heights, one can predict the input spectrum at the top of an exoplanet's atmosphere for earlier and later times in the host star's evolution by perturbing the stellar model to fit the emission-line fluxes (e.g., Ca II, Hα, Mg II) observed in stars with different ages (see Engle, Guinan, & Mizusawa 2009). Understanding the radiative output of host stars and its effects on habitability is essential for identifying the best targets for future studies of exoplanet atmospheres. Stellar models also permit us to compute the net cooling rates that theoretical models must eventually explain by predicting the required heating rates at each height and temperature.

Although there are extensive grids of theoretical models of cool star photospheres computed assuming convective-radiative equilibrium, for example the PHOENIX models and their revisions (e.g., Allard & Hauschildt 1995; Allard et al. 2001; Hauschildt & Baron 2008; Allard et al. 2010) and the MARCS models (Gustafsson et al. 2008), these models are inadequate for predicting stellar UV spectra. Maldonado et al. (2015) summarize the present state of photospheric models of cool stars and provides useful intercomparisons. Existing photospheric models fail by orders of magnitude to predict the continuum and line flux below 250 nm emitted by the chromosphere and corona (cf. Loyd et al. 2016) where nonthermal heating determines the thermal structure. Non-LTE line formation is also needed to explain the observed line profiles and fluxes. Most observed M, K, and G stars, and even F types, have upper chromospheres and transition regions in which nonradiative

heating, most likely by the conversion of magnetic energy to heat, raises temperatures far above the radiative-convective equilibrium predictions. This heating decreases the molecular abundances in a way that can be confused with a lower stellar metallicity.

Previous chromospheric models for M dwarf stars were usually computed to fit only the Ca II, Hα, and Na I D lines (e.g., Mauas et al. 1997; Houdebine & Stempels 1997; Short & Doyle 1998; Fuhrmeister, Schmitt, & Hauschildt 2005; Houdebine 2009, 2010a,c). An exception is the M-dwarf flare models computed by Hawley & Fisher (1992) that fit the observed X-ray emission and transition-region lines in addition to the chromospheric lines. Although emission in the cores of the Ca II H and K lines indicates the presence of nonradiative heating in the upper chromosphere, these lines are insufficient for predicting the temperature structure above 7,000 K and thus most emission lines at wavelengths shorter than 300 nm. With a semi-empirical non-LTE model, Avrett et al. (2015) fitted the UV continuum and line spectrum of a sunspot, which may have a thermal structure similar to a relatively inactive M0 V star but with different gravity, very strong magnetic fields, and external illumination from the normal solar atmosphere. Given these differences between a sunspot and an M dwarf and the importance of exoplanet studies, we compute a semi-empirical model for a representative M dwarf to fit an excellent panchromatic data set.

We have selected for modeling GJ 832 (HD 204961), a nearby M2 V (Maldonado et al. 2015) red dwarf star located at a distance, $d = 4.95 \pm 0.03$ pc (van Leeuwen 2007). The age of this star is not well constrained observationally, but there are clues that the star is not young and perhaps as old as the Sun. Its measured rotational period, $P_{\rm rot} = 45.7 \pm 9.3$ days, (Suárez Mascareño et al. 2015) and Hα absorption rather than emission indicate a low level of activity. West et al. (2015) finds that stars with such rotational periods are likely members of a kinematically older population. Newton et al. (2016b) finds that the mean kinematic age of M dwarfs observed in the MEarth program

with rotation periods in the range 10–70 days is 3.1 Gyr, but this result is uncertain due to the small number of stars in the group. France et al. (2013) showed that the UV spectrum of GJ 832, including the Ly-α, C IV, and Mg II fluxes, is consistent with chromospheric and transition-region measurements of other intermediate age M dwarfs. Estimates of the stellar properties of GJ 832 are mass, $M = 0.45 M_{\odot}$ (Bonfils et al. 2013), radius, $R = (0.499 \pm 0.017) R_{\odot}$ (Houdebine 2010a), luminosity, $L = 0.026 L_{\odot}$ (Bonfils et al. 2013), and surface gravity, log g = 4.7 (Schiavon, Barbuy, & Singh 1997). For these values of the stellar radius and distance, the solid angle of the star observed at its distance from Earth is $\Omega_{*} = \pi(R/d)^2 = 1.622 \times 10^{-17}$ steradians, and the solid angle of the star viewed at a distance of 1 Astronomical Unit (1 AU) is $\Omega_{\rm 1AU} = \pi(R/1AU)^2 = 1.691 \times 10^{-5}$ steradians. We will use these quantities later in the paper to convert from average disk intensity to flux units and compare with solar models.[3]

GJ 832 hosts a $0.64 M_{\rm Jup}$ exoplanet (Bailey et al. 2009; Wittenmyer et al. 2014) with a relatively long orbital period, $P = 10.01 \pm 0.28$ years, at a mean distance from the star, $a = 3.56 \pm 0.28$ AU. Wittenmyer et al. (2014) discovered that this star also hosts a super-Earth at a mean distance, $a = 0.162 \pm 0.017$ AU, with an orbital period, $P = 35.67^{+0.15}_{-0.12}$ days. This exoplanet, lies just inside the inner edge of the habitable zone, but given its large mass, $M > 5.4\ M_{\rm Earth}$ and likely large greenhouse atmosphere, Wittenmyer et al. (2014) suggested that it is more likely a very hot super-Venus.

Although it is difficult to obtain accurate metallicities for M dwarfs, Bailey et al. (2009) derived [Fe/H] $= -0.31 \pm 0.2$ for GJ 832 using the photometric metalicity calibration of Bonfils et al. (2005). Subsequently, Johnson & Apps (2009) estimated the metallicity to be slightly subsolar ([Fe/H] = –0.12) by using a grid of convective-radiative LTE atmospheric

[3]The stellar radius may have a large uncertainty. If R is as large as $0.52 R_{\odot}$ (see Section 3.1), then Ω_{*} and Ω_{1AU} increase by 8.6%.

models to fit the infrared FeH feature. In Section 3.2, we examine the issue of metal abundances of this star in light of the new physical model with a warm upper chromosphere.

In Section 2, we describe our approach and the resulting physical model. In Sections 3 and 4, we compare the computed spectrum with observations, and in Section 5 we compute the contribution functions for the important spectral lines and radiative losses as a function of wavelength and temperature as a guide to future theoretical heating models. In this section, we also discuss where spectral lines are formed in the M-dwarf model and the similarities and differences between the M-dwarf model and solar models. Section 6 is our summary of this investigation and our conclusions.

2. PROCEDURE FOR CALCULATING NON-LTE ATMOSPHERIC MODELS AND EMERGENT SPECTRA

Our approach is to model the temperature versus pressure distribution in the atmosphere of GJ 832 based on the star's observed spectrum. This approach departs from the classical grids of stellar atmospheric models based on purely theoretical considerations of convective-radiative energy transport (e.g., ATLAS9, MARCS, and PHOENIX) as described and intercompared by Bozhinova, Helling, & Scholz (2015), but is similar to our approach used for computing semiempirical models of the solar atmosphere as described more fully in the next paragraph. We begin our calculations with an existing photospheric model for a star with similar spectral type and luminosity as GJ 832. We then substantially modify this thermal structure in the lower chromosphere and extend the temperature-pressure distribution from the temperature minimum to the corona to match the observed spectrum. Given the complexity of our model atmosphere code needed to properly compute statistical equilibrium and radiative transfer in very many transitions, we assume a one-dimensional geometry. The first models of M dwarfs with a three-dimensional

geometry are now being computed (Wedemeyer, Ludwig, & Steiner 2013), but such models must make approximations in the radiative transfer physics and completeness that our model does not make.

We compute stellar spectra in full non-LTE using the Solar-Stellar Radiation Physical Modeling (SSRPM) tools. These tools are an offspring of the Solar Radiation Physical Modeling (SRPM) system developed in the course of five papers: Paper I (Fontenla et al. 2007), Paper II (Fontenla et al. 2009), Paper III (Fontenla et al. 2011), Paper IV (Fontenla et al. 2014), and Paper V (Fontenla et al. 2015). The SRPM system computes one-dimensional solar atmosphere physical models (distributions of temperature and density with pressure) in full non-LTE for each of the features observable on the solar disk and synthesizes from the models their emitted radiation. This modeling of the entire solar atmosphere from the photosphere to the corona produced very high-resolution spectra ($\lambda/\Delta\lambda \sim 10^6$) that we then tested against ground- and space-based spectra of the solar disk center at very high resolution to refine the models. The models also reproduce observations of the Sun as a star, the solar spectral irradiance (SSI), including the UV spectra observed by a number of spacecraft with good absolute flux calibration. The most recent models described in Paper V now accurately fit the solar 160–400 nm irradiance that previous models had great difficulty fitting. The SRPM tools, therefore, provide a very solid platform upon which we added to SSRPM a more extensive calculation of molecular formation in LTE that includes molecular sequestration of elements and an improved list of the molecular lines that are most important for M-dwarfs, e.g., TiO, using data from Plez (1998).

SSRPM calculations currently include 52 atoms and ions in full-NLTE, in addition to H, H^- and H_2. The effectively thin approximation is used for an additional 198 highly ionized species. In total, we consider 18,538 levels and 435,986 spectral lines produced by atoms

and ions. Also included are the 20 most-abundant diatomic molecules and about 2 million molecular lines. As described in Paper V, we use new photodissociation cross-sections of the important species. Radiation in the lower layers is computed in a plane-parallel approximation and the coronal radiation in a spherically symmetric approximation. The inclusion of optical data (see Section 3.1) allows us to obtain consistent models that constrain the photospheric structure and visible to IR wavelengths. The inclusion of UV emission lines originating in the chromosphere and transition region and coronal X-ray data allows us to create a self-consistent physical picture of the complete M dwarf atmosphere and spectrum from 0.1 nm to 300 microns.

Our calculations use an iterative linearization scheme to solve the nonlinear molecular LTE equilibrium equations. For each general iteration in the present scheme, the linearized simultaneous equations for molecule formation are solved in a subiteration block, and the full non-LTE level populations and ionization states are solved for all neutrals and ions in a separate subiteration block. We normalize densities to the elemental abundances, which the present model assumes to be solar. These elemental abundances are listed in Papers III-V. We note that coronal abundances may differ from those lower in the atmosphere, the so-called FIP effect.

Qualitatively, the star's atmospheric model is based on our experience in modeling the Sun, but its physical values are very different. The conversion of the absolute measurement of the stellar spectrum flux at Earth to the stellar average-disk intensity is carried out as in Fontenla et al. (1999) and depends on the accuracy of the stellar radius-to-distance ratio. Since the distance to the star is known to better than 1%, the stellar radius dominates the uncertainty. The color index B–V = 1.52 (Bailey et al. 2009) points to a photospheric temperature $T \sim 3600$ K (Bessell 1995), while Maldonado et al. (2015) estimate $T_{\rm eff} = 3580 \pm 68$ K. In the present study, we assume the value of gravity at 5×10^4

cm s^{-2}, and radius, $R = 0.499 R_{\odot}$ (Houdebine 2010a).

In the top panel of Figure 1, we compare the temperature versus gas pressure distribution for GJ 832 (model 3346) to that for the quiet Sun inter-network model 1401 computed in Paper V. The models are quantitatively very different, but there are many qualitative similarities. Both models have a photosphere and lower chromosphere in which temperature decreases outward with decreasing pressure. After reaching a minimum, the temperature in the upper chromosphere rises rapidly beginning at a pressure $P \approx 15$ dynes cm^{-2} in the GJ 832 model and $P \approx 40$ dynes cm^{-2} in the solar model, reaching a plateau with nearly constant temperature followed by a steep temperature rise in the transition region. Like solar models, model 3346 includes a geometrically thin transition region and a geometrically extended corona with a maximum temperature of approximately 2.7 MK (see Section 3.5), which is significantly hotter than in models for the quiet-Sun inter-network (model 1311) but is similar to the solar corona in the bright plage model 1315 (computed in Paper IV) as shown in the bottom panel of Figure 1. We plot temperatures versus height for the transition region and coronal layers, since the pressure is nearly constant with height in these hot layers.

The thermal structure of the atmospheric model of GJ 832 is quantitatively very different from the Sun, in particular model 3346 has a much cooler photosphere and chromosphere and higher pressure in the transition region than in the quiet Sun model. As a result, the spectral features of GJ 832 have different fluxes than the Sun. The FUV spectra observed by *HST* provide important constraints on the transition region that we discuss below. The detailed structure of the coronal portion of the GJ 832 model is mostly theoretical and results from the very high thermal conductivity of coronal plasma. We use the total X-ray luminosity and the Fe XII 124.2 nm line to constrain the energy deposited in the corona and the energy balance calculations to determine the temperature structure

of the corona of GJ 832.

The photospheric and lower-chromospheric layers are derived from the visible spectrum and do not differ significantly from convective-radiative standard models, for example the PHOENIX models. However, extending the lower-chromosphere temperatures further out in the atmosphere completely fails to reproduce the UV emission lines of ionized species. The GJ 832 model includes a steep temperature rise with decreasing pressure begining at $P \approx 15$ dynes cm^{-2}. The pressure at which this chromospheric temperature rise occurs was first estimated by considering the triggering of the Farley-Buneman instability (see Fontenla et al. 2007) and a magnetic field of about 100 Gauss, which is representative of typical values for the magnetic field observed in the quiet Sun. Above the upper-chromospheric "plateau" with nearly constant temperature, there is a sharp rise to a coronal temperature $T \approx 2.7 \times 10^6$ K (see Section 3.5) with little change in pressure because of the small geometric thickness of the transition region. The steepness of the transition region is determined from matching the emission lines in the observed 100–200 nm spectrum using the methods described in Paper II with detailed calculations of the radiative losses by H and all other species (see Section 5.2) based on the recent atomic data from CHIANTI 7.1 (Landi et al. 2013).

3. COMPARISON OF OBSERVED AND COMPUTED SPECTRA

We now compare the observed spectrum of GJ 832 with the spectral synthesis of our model 3346. For this we use the "average disk intensity" (units erg s^{-1} cm^{-2} nm^{-1} sr^{-1}) as defined by Fontenla et al. (1999, Appendix B), which is equivalent to the "astrophysical flux" at the stellar surface (cf. Mihalas 1978). The average disk intensity is a property of the star's atmosphere (independent of stellar distance and radius) and is converted to the physical flux measured at Earth by a conversion factor that is the inverse of the stellar

angular diameter, $\Omega_* = \pi(R/d)^2$, where R is the star's radius, and d the distance from Earth to the center of the star. Using these values as mentioned above, we establish the conversion factor of $1/\Omega_* = 6.165 \times 10^{16}$ sr^{-1}. The conversion between astrophysical flux traditional units and SI units is simply: 1 W m^{-2} nm^{-1} sr^{-1} = 100 erg cm^{-2} s^{-1} Å^{-1} sr^{-1}.

3.1. The Visible Spectrum

We analyze the optical spectra of GJ 832 observed on Sept 1 and 15, 2012 with the REOSC cross-dispersed echelle spectrograph on the 2.15 m Jorge Sahade telescope at the Complejo Astronomico El Leoncito (CASLEO) in Argentina. The REOSC spectrum was flux calibrated by assuming that it is similar to that of a reference M1.5 V star (GJ 1), which was calibrated according to the procedure developed by Cincunegui & Mauas (2004). The calibration procedure in that paper was estimated to have a 10% uncertainty but it is not well established how GJ 832 may differ from GJ 1, implying that the absolute flux calibration uncertainty may be larger than 10%.

The observed visual spectrum wavelengths have been converted to vacuum wavelengths for comparison with the model spectrum, which was smoothed to the resolution of the CASLEO REOSC spectrograph of $\lambda/\Delta\lambda = 13,000$ (2 pixels). Evans et al. (1961) published a radial velocity of 4.1 km s^{-1} for this star, but the moderate resolution of the CASLEO REOSC spectrograph does not allow for a very accurate wavelength scale and we have not applied this small Doppler shift to the observations.

The observed and computed spectra between 400 nm and 675 nm are shown in Figure 2. This figure shows that the adopted set of parameters and physical model are broadly consistent with the observed intensities, although some minor differences occur.

3.1.1. Continuum Intensity

Our experiments varying the photospheric temperature distribution show that the overall shape of the visible spectrum depends very little on the photospheric temperature gradient but much more on the temperatures at photospheric pressures. For solar-type stars, the layer at which optical depth is unity in the radial direction at the continuum wavelength of 500 nm is often used as a reference height. This reference height is not practical for M-type stars, because many spectral lines and the continuum cannot be isolated in medium-resolution spectra such as those obtained with the CASLEO REOSC.

While optical depth unity ($\tau = 1$) is a representative height for the observed photospheric emission at solar disk center, $\tau = 2/3$ corresponds to optical depth unity at the mean observing angle ($\mu = 2/3$) for an unresolved star and is more representative of the average disk intensity or emitted flux. We therefore consider $\tau = 2/3$ as the approximate location for stellar emission. The observed pseudo-continuum is much lower than the theoretical real continuum because of the "jungle" of overlaping molecular absorption lines, mostly TiO lines, that cannot be separated even in high-resolution spectra. The molecular line features that are discernable in the CASLEO spectrum correspond to exceptionally high transition probabilities, and are less well defined in the observed spectrum than in our computated spectrum, because we include only micro-turbulent line broadening and stellar rotation velocities. Other velocities would smear the model spectrum but do not affect the conclusions of the present paper. For instance, in our high-resolution spectrum near 650 nm, the highest flux occurs at $\tau = 2/3$, where the pressure $P_{\rm phot} \sim 1.8 \times 10^5$ dyne cm^{-2} and the temperature $T_{\rm phot} \sim 3440$ K. However, at the bottom of the nearby spectral lines, $\tau = 2/3$ occurs higher in the atmosphere at $P \approx 2.6 \times 10^4$ dyne cm^{-2} and $T \approx 3000$ K. In a calculation that excludes molecular lines but uses the same physical model, we find that the true continuum formed near $\tau = 2/3$ occurs at $P_{\rm phot} \sim 2.8 \times 10^5$

dyne cm^{-2} and $T_{\rm phot} \sim 3570$ K. However, the highest intensity level between spectral lines is significantly below the true continuum, which cannot be observed in the visible spectrum even at extremely high spectral resolution because of line blending.

3.1.2. Ca II H and K, Na I D, TiO lines, and Hα

Figure 3 shows spectral lines from several atoms, ions, and TiO molecules. Particularly interesting are the visible lines that can display stellar activity, including Ca II H and K and Hα. Although relatively weak in less active M dwarfs, these lines in GJ 832 indicate the presence of a nonradiatively heated upper chromosphere and are, therefore, valuable proxies for the UV flux and stellar activity cycles in M dwarfs. The upper left panel in Figure 3 shows that the observed Ca II lines are well matched by our model. The computed line centers of the Ca II H and K lines form in the upper chromosphere (see Section 5.1) in the temperature range 4,000–20,000 K and pressure range 1–10 dynes cm^{-2}, which is similar to the formation temperature range in the quiet Sun. In the GJ 832 model, Ca is essentially neutral throughout the cool lower chromosphere and, as a result, the Ca II lines do not have the very broad absorption wings that are formed in the Sun's much warmer lower chromosphere (see Fig. 3). In the upper chromosphere, Ca II is sufficiently abundant to produce observable emission cores but no significant absorption wings. Therefore, the Ca II lines in GJ 832 are very different from the solar spectrum where these lines have very broad absorption wings but only weak central emissions.

Among other absorption lines also displayed in this panel, the deepest are the Al I resonance lines at 394.512 and 396.264 nm that are also very prominent in solar spectra. The central intensities and widths of the Al I lines are well fit by our model, and these lines are much broader than observed in solar spectra, because Al is primarily neutral in the photosphere and lower chromosphere of GJ 832.

Other lines from neutral species, for instance the Na I D1 and D2 lines, are prominent absorption lines formed in the lower chromosphere. The upper right panel in Figure 3 shows that the observed and computed cores and wings of the Na I lines are in excellent agreement. The plot also shows that not including absorption by the many TiO lines would produce a very poor fit to the Na I line wings and adjacent continuum. Another important absorption line in this panel is the Ca I 585.907 nm line that our model fits very well.

The visible spectrum of GJ 832 is largely dominated by TiO absorption lines, as is typical for M-type stars and, to a lesser extent, for sunspots. These and other molecular lines distort the shape of the underlying continuum. The lower left panel in Figure 3 shows a portion of the important TiO bands, indicating that our model produces good agreement in this particular band. We cannot, therefore, make a statement concerning the metal abundances based only on the TiO lines, but we can say that they are not inconsistent with the solar abundances we used.

The lower right panel in Figure 3 shows that the observed and computed Hα line depths are in excellent agreement only when the many TiO lines are included. An analysis of the Hα line formation indicates that the line is formed essentially in the upper chromosphere where the first-excited level population of hydrogen produces the Hα absorption. This panel also shows the strong Ca I 657.459 nm line whose line center is underestimated, likely due to poor atomic data for some of the Ca I lines.

3.2. Molecular Formation and Metallicity

Our computed spectrum is based on the solar abundances listed in Paper V, and the relatively small differences between the computed and observed TiO lines rule out a large difference between the solar and stellar abundances of Ti and O. If the abundances of

these elements in GJ 832 were substantially smaller than solar, then the general slope of the spectra and the depth of the TiO bands would not be as close to the observations as our computations show. Also, significantly subsolar abundances would make it difficult to match the observed Ca II, Mg II, and many other lines.

The inclusion of a chromosphere in our model leads to a good fit to many, but not all, of the observed spectral features of GJ 832. We find that the metal abundances in this star are consistent with or slightly lower than solar, for example log[Fe/H]=–0.12 (Johnson & Apps 2009) and -0.17 ± 0.17 (Maldonado et al. 2015). Johnson & Apps (2009) argue that the photometric-based metallicity determinations for M dwarfs, e.g., log[Fe/H] = –0.31 for GJ 832 (Bailey et al. 2009), systematically underestimate these metallicities. Also, the abundance estimate by (Bailey et al. 2009) would reduce by a factor of 4 the depths of the TiO lines, which depend on the square of the metallicity, and would also decrease the absorption in all other spectral lines, making it very difficult to match the observed spectra.

Figure 4 shows some molecular and atomic densities computed in the present model of GJ 832. For the elements shown here, the ionization remains very low in the photosphere and lower chromosphere, facilitating the formation of molecules from neutrals. The left panel in Figure 4 shows that atomic and molecular H have nearly equal abundance throughout the photosphere. However, the H_2 density decreases rapidly as the temperature increases and density decreases toward the upper chromosphere. In these layers ionized H dominates over H_2. Despite the temperature increase, H remains mostly neutral in the lower and upper chromosphere. Unlike the Sun, H ionization in GJ 832 remains small even in the upper chromosphere, and its contribution to the electron density is much smaller than in the Sun. The right panel of Figure 4 shows C densities in several forms. Notably throughout the photosphere and lower chromosphere, CO dominates, leaving very little C in other forms. With increasing temperature and decreasing density in the upper

chromosphere, the CO density decreases rapidly and neutral C atoms dominate, except close to the top of the upper chromosphere where ionized C slightly dominates.

3.3. Near Ultraviolet Spectrum

France et al. (2013) described the NUV spectra of GJ 832 obtained with the STIS instrument on *HST* on 2012 Apr 10 and 2012 Jul 28. The NUV spectrum (157–315 nm) was obtained with the G230L grating, which has low spectral resolution ($\Delta v \approx 600$ km s^{-1}). The Mg II lines were also observed at high resolution ($\Delta v \approx 2.6$ km s^{-1}) with the E230H grating that includes the 267–295 nm spectral region.

These data were calibrated to disk average intensity using the nominal calibration factor 6.165×10^{16} sr^{-1} and Doppler-shifted to match the computed spectrum wavelengths. To match the resolution of the observed spectrum with the computed line widths, we convolved the computed spectrum with a cos^2 filter of 0.3 nm FWHM. The faint continuum is not well measured at wavelengths shorter than $\sim$ 220 nm, but is well detected in the MUSCLES Treasury Survey data (Loyd et al. 2016).

The observed and computed spectra in the 210–300 nm NUV range are shown in Figure 5. This figure shows the Mg II h and k lines for which the observation and the model agree well after the observed fluxes are increased to account for interstellar absorption as described below. These lines were used to adjust the model's upper chromosphere and transition region. We computed the Mg II and Ca II lines by merging the atomic levels of each ion that have the same quantum numbers, except for the total angular momentum (J), into superlevels and assumed that the relative populations of the sublevels are in LTE. This joining together of levels is often used to reduce the size of the system of equations while including many excited states. However, in low density layers, this approximation is

inaccurate, leading to one emission line of the multiplet being too bright and the other too faint compared to the calulated intensities for the merged state.

In the model for GJ 832, the line centers of the Mg II lines (at the calculation's highest resolution) form near $T = 7000$ K at a pressure of $P \approx 0.6$–0.8 dyne cm^{-2}, but the emission peaks on either side of line center are formed mostly at lower temperatures (and higher pressures). The Mg II lines of GJ 832 do not display absorption wings (see Figure 6), because there is very little singly ionized Mg in the cool lower chromosphere. The Mg II line cores in GJ 832 are narrow because Mg II is the dominant ionization stage only in the upper chromosphere and transition region.

The high-resolution Mg II spectra obtained with the STIS E230H grating were calibrated to average disk intensity using the nominal calibration factor and corrected for a Doppler shift of 12 km s^{-1}. Figure 6 shows the observed and computed high-resolution spectra of the Mg II h and k lines. The computed and observed fluxes are roughly in agreement, but the computed profile shapes at line center show a double-peaked upper-chromospheric component with a relatively strong central reversal. The observed line shape, however, shows only a double-peaked profile with a pronounced central dip.

We believe that the observed shapes of the Mg II line profiles can be explained as a superposition of a weak-chromospheric central reversal computed using model 3346 and interstellar Mg II absorption at nearly the same wavelength. The Redfield & Linsky (2008) model of the local interstellar medium predicts that the line of sight to GJ 832 (radial velocity 4.3 km s^{-1}) likely passes through four interstellar clouds. According to the kinematic calculator based on this model,[4] the cloud velocitites for this line of sight are LIC (-11.3 km s^{-1}), Aql (+8.5 km s^{-1}), Mic (-15.1 km s^{-1}), and Vel (-17.0 km s^{-1}).

[4]http://lism.wesleyan.edu/LISMdynamics.html

The predicted absorption by the three clouds at negative radial velocities would occur at –0.015 nm to –0.020 nm from line center and may be detected as weak absorption just to the left of the emission line. Absorption by the Aql cloud should occur at +4.2 km s^{-1} or 0.004 nm from line center. This interstellar absorption could add to the central dip in the k line and the asymmetry with the blue peak slightly stronger than the red peak. We think that this combination of the weak self-reversal predicted by model 3346 and interstellar Mg II absorption is the most likely explanation for the Mg II line profile shapes, and to compensate for the interstellar absorption we increase the observed flux of the Mg II lines listed in Table 1 by 30% (see France et al. 2013, Figure 5). The observed fluxes of the Mg II and other spectral lines at a distance of 1 AU from the star are compared in Table 1 with the line fluxes computed for the GJ 832 and the quiet and active Sun models.

Figure 5 shows that the formation of the Mg I 285.2 nm line is a problem for the present model as the calculated emission is far larger than observed. We find that the Mg I emission forms over the bulk of the upper chromosphere from its base pressure $P \approx 15$ dyne cm^{-2}, up to its top pressure $P \approx 0.8$ dyne cm^{-2}, which produces a wide emission line. We found that slight changes in temperature and shape of the upper chromosphere can decrease the Mg I emission, since a slight increase in the temperature of this layer could produce a better balance between the Mg II and Mg I lines while maintaining the good agreement with the observed Ca II lines. However, we could not eliminate the strong Mg I emission, and in Section 5.4 we argue that uncertain atomic ionization rates are the more likely explanation for the computed Mg I emission feature.

Many other lines shown in Figure 5 show good agreement between the calculations and the observations. Particularly important are the many Fe II emission lines in the ranges 232–242 and 260–265 nm. Emission in these lines would have important effects on O_3 for any potentially habitable exoplanets around GJ 832 (see Tian et al. 2014).

H_2 spin-forbidden transitions are likely an important opacity source in the 240–310 nm region. Unfortunately, there are no *ab initio* calculations for this opacity source, and in Paper V we estimated the strength of the H_2 opacity needed to best fit the 160–300 nm quiet-Sun spectrum. However, we find that this strength for the H_2 opacity is too large for GJ 832 that has lower temperatures than the quiet-Sun model 1401. Different assumptions regarding the H_2 opacity greatly affect the NUV continuum intensity in the range 245–310 nm. However, the required amount of H_2 opacity is closely connected with the plausible NLTE formation of H_2 near the temperature minimum, which we will address in a future paper.

3.4. The Far-ultraviolet Spectrum

France et al. (2013) described the FUV spectra of GJ 832 obtained with the COS and STIS instruments on 2011 Jun 9 and 2012 Jul 28. The COS G130M and G160M gratings observed the 114–179 nm spectral region with a resolution $\Delta v \approx 17$ km s^{-1}, and the STIS E140M grating observed the 114–171 nm spectral resolution with a resolution $\Delta v \approx 7.5$ km s^{-1}. We find very good agreement between the calculated and observed FUV emission lines shown in Figure 7.

In our model, the peak in the contribution function for the C II 133.4 nm line center is near 20,000 K (see Section 5.1), and the peak contibution function for the Si IV 139.3, 140.3 nm doublet is near 40,000 K. The O IV] semi-forbidden 140.1 nm line, which forms at temperatures around 160,000 K, is well fit by our model. The C IV 154.8, 155.1 nm doublet peak contribution is at 100,000 K and the N V 123.9, 124.3 nm doublet peak is at 170,000 K, but both form over a wide range in temperature.

Table 1 shows the fluxes of observed FUV emission lines at a distance of 1 AU from the

star compared to the spectral synthesis intensities computed from the models for GJ 832 and the quiet and active Sun. For the C II 133.45 and 133.57 nm lines, we have corrected the observed fluxes for an assumed 30% absorption by interstellar C II, similar to our correction for the Mg II lines. The computed fluxes of the transition region lines (Si IV, C IV, O IV], and N V) all lie within 20% of the observed fluxes. For the lines formed in the chromosphere and lower transition region (Ly-α, Mg II, Ca II, and C II), the agreements with the observed line fluxes are mostly within 50%.

The Ly-α line (Figure 8) presents a special case of an optically thick line with broad wings and significant interstellar absorption. We compare in Figure 8 the model 3346 profile with the observed profile. Interstellar absorption by H I Lyman-α and, to a lesser extent, D I Ly-α centered at –0.033 nm from the H I line absorb most of the intrinsic stellar emission line and severely distort its shape. To obtain a qualitative assessment of the accuracy of the emission line computed from model 3346, we compare the computed line with the observed line corrected for interstellar absorption. There are two techniques now utilized for reconstructing the Ly-α line: (1) using the interstellar absorption profiles of the D I Ly-α and metal lines to infer the H I absorption (Wood et al. 2005), and (2) a self-consistent solution for the interstellar absorption parameters and the intrinsic stellar emission line that best fits the observed line profile (France et al. 2013; Youngblood et al. 2016). Allison Youngblood has kindly reconstructed the observed Ly-α line (shown in Figure 8) with an integrated flux of 3.86 ergs cm^{-2} s^{-1} at 1 AU using the technique described in the Youngblood et al. (2016) paper. Using an earlier version of this technique, France et al. (2013) obtained an integrated flux of 5.21 ergs cm^{-2} s^{-1}. By comparison, the integrated flux of the computed line is 2.13 ergs cm^{-2} s^{-1}. Given the signal-to-noise of the observed profile and the uncertainties in the reconstruction technique, we conclude that the model 3346 Ly-α flux is consistent with the reconstructed stellar line flux.

The wings of the computed Lyman-α line are somewhat broader than the reconstructed profile. This may result from uncertain atomic data for carbon, because C I bound-free opacity and C II recombination overlap the Lyman-α wings.

There is an interesting trend in the relative line fluxes with line-formation temperature between GJ 832 and the quiet and active Sun. The line flux ratios for model 1401 divided by the observed GJ 832 fluxes decrease from 128 for Mg II, to 12.1 for the combined C II, Si IV, and C IV lines, to 3.08 for the highest temperature N V lines. The corresponding flux ratios for model 1401 divided by model 3346 are similar: 125 for Mg II, 13.0 for the combined C II, Si IV, and C IV lines, and 3.0 for the N V lines. The increased flux of the high-temperature lines compared to low-temperature lines results from the steep temperature rise into the transition region occuring at nearly an order of magnitude larger pressure in GJ 832 model than in the quiet Sun model. We note that a similar displacement of the transition region to higher gas pressures occurs in solar models for regions of higher magnetic activity and in previouly computed active M-dwarf models (e.g., Houdebine & Stempels 1997; Walkowicz & Hawley 2009). Models of solar active regions (e.g., model 1404) have both higher gas pressures, which greatly increase the emission line intensities, and steeper temperature gradients in the transition region, which partially reduce the increased intensities.

Model 3346 for the transition region of GJ 832 was verified and computed using the 0.8 dyne cm^{-2} base pressure and a similar energy deposition and flux limiting, as described in Papers II and III, respectively. The resulting model of temperature vs height for the transition region lies between solar models 1303 and 1304.

3.5. The X-ray and EUV Spectra

Figure 9 shows the complete 0–200 nm spectrum of GJ 832 computed by adding the intensity from the upper layers to that emitted by the lower part of the complete model. This procedure assumes that the upper part of the model is optically thin at all UV wavelengths, which is a fair assumption considering the small coronal optical depths.

The upper transition region and corona of our GJ 832 model are defined by theoretical considerations of energy balance and the strong constraints imposed by observations of the C IV (T=100,000 K) and N V (T=170,000 K) lines formed in the lower transition region. This theoretical method was first described by Rosner, Tucker, & Viana (1978) and was addressed by Fontenla, Avrett, & Loeser (2002) and references therein. Martens (2010) then developed an analytical model consistent with this theoretical method using parametric forms for the radiative losses and coronal heating. In Papers IV and V we presented a set of models for various regions of the Sun with models 1401/1311 describing the average quiet Sun (feature B) and models 1404/1314 describing a moderately active region of the Sun (feature H). The line intensity ratios in the GJ 832 FUV spectrum are similar to a slightly less active plage than feature H in the Sun and are consistent with a pressure of $P = 0.8$ dyne cm^{-2} and a heat flux of $\sim 2 \times 10^6$ erg cm^{-2} s^{-1} at 200,000 K.

Our model for GJ 832 is based on the same theoretical principles as the solar models with the observed constraints for GJ 832 in a spherically symmetric geometry, because the corona extends for a significant fraction of the stellar radius. The resulting detailed structure of the model is similar to that of the moderate activity solar plage (feature H in the Sun), except that the model corona for GJ 832 is slightly hotter and less extended than that of feature H on the Sun. These differences may be explained by the higher gravity of GJ 832 compared to the Sun. We note that Chadney et al. (2015) calculated X-ray and EUV spectra of the the more active M dwarfs AD Leo and AU Mic that are similar to

model spectra of the more active Sun than to the quiet Sun.

The Fe XII 124.20 nm magnetic dipole line was first detected in the Sun by Burton, Ridgeley, & Wilson (1967) and subsequently in α Cen A (G2 V) (Pagano et al. 2004) and ϵ Eri (K2 V) (Jordan et al. 2001). This line, shown in Figure 7, forms at a temperature near 1.4 MK (see the right panel of Figure 11), which is too cool to be in the corona of our model of GJ832 or in the solar feature H. Instead, as shown in Fig. 1, this line forms in the upper part of the transition region.

Sanz-Forcada et al. (2010) reported an X-ray luminosity for GJ 832 of $L_X = 6.02 \times 10^{26}$ erg s^{-1} integrated over the band 0.1–2.4 keV (i.e., 0.515–12.4 nm) based on the measured *ROSAT* X-ray flux. This X-ray luminosity corresponds to a surface physical flux of 3.88×10^5 erg s^{-1} cm^{-2} (assuming a stellar surface area of $0.25 A_\odot = 0.25 * 1.52 \times 10^{22} = 3.80 \times 10^{21}$ cm^2) and an integrated average disk intensity of 1.55×10^4 erg s^{-1} cm^{-2} sr^{-1}, which is ~ 10 times that of the quiet Sun model 1401 computed in Paper V. However, the GJ 832 average disk intensity in this band is intermediate between that of the solar bright network and the weak active-region models (1403 and 1404, respectively).

Recently, Loyd et al. (2016) observed GJ 832 with the EPIC instrument on *XMM-Newton* as part of the MUSCLES Treasury Survey Program. They found that the X-ray spectral energy distribution can be fit by a two-component model with temperatures $kT_1 = 0.09^{+0.02}_{-0.09}$ keV and $kT_2 = 0.38^{+0.11}_{-0.07}$ keV, corresponding to $T_1 \approx 1.04 \times 10^6$ K and $T_2 \approx 4.41 \times 10^6$K. The corresponding volume emission measures are $VEM_1 \approx 2.4 \times 10^{49}$ cm^{-3} and $VEM_2 \approx 0.5 \times 10^{49}$ cm^{-3}. The coronal temperature at the top of our one-component model lies between these two temperatures and $\log L_X = 26.26 \pm 0.05$ ergs s^{-1}(Loyd et al. 2016). The earlier *ROSAT* X-ray luminosity $\log L_X = 26.78$ cited by Sanz-Forcada et al. (2011) is a factor of 3.3 larger than the *XMM-Newton* measurement.

The lower panel of Figure 9 compares the observed *XMM-Newton* spectrum in the

0.7–5.0 nm range with model spectra for GJ 832 (model 3346), the quiet Sun (model 1401), and a solar plage (model 1404). Since the resolution of the EPIC spectrometer on *XMM-Newton* is much lower than the plotted model spectra ($\lambda/\Delta\lambda \approx 5$ in the middle of the spectral range), the observed spectrum is smoothed to 0.6 nm FWHM for comparison with the model spectra. The agreement of the spectral energy distributions of the observed and model X-ray spectra demonstrates that our model can be used to approximently represent the X-ray and the unobservable EUV spectrum of GJ 832. We note, however, that coronal emission of more active M dwarfs can be highly variable, and both the *ROSAT* and *XMM-Newton* observations were obtained at different times than the UV measurements.

The integral of the average disk intensity in our model between 10 and 91.2 nm is 6.21×10^{-13} erg s^{-1} cm^{-2} sr^{-1}, of which 36.4% is emission from the chromosphere and lower transition region and 63.6% is from the upper transition region and corona. The corresponding flux at Earth is $f_{\rm EUV} = 6.21 \times 10^{-13}$ erg s^{-1} cm^{-2} and the luminosity is $\log L_{\rm EUV} = 27.26$ erg s^{-1}. From the X-ray flux observed with *ROSAT*, Sanz-Forcada et al. (2011) computed $\log L_{\rm EUV} = 27.83$ erg s^{-1}. This EUV luminosity is a factor of 3.7 larger than computed from our model, but the *ROSAT* X-ray flux upon which it is based is a factor of 3.3 larger than the *XMM-Newton* flux, indicating that GJ 832 was more active at this earlier time. The scaling between EUV and X-ray luminosity in eq. 3 of Sanz-Forcada et al. (2011) predicts that the EUV luminosity at the time of the *XMM-Newton* observation would be $\log L_{\rm EUV} = 27.38$. A third method for computing the EUV emission is scaling from the Ly-α flux (Linsky, Fontenla, & France 2014). Youngblood et al. (2016) obtained $\log L_{\rm EUV} = 27.45$, but this number includes emission in the 91.2–117 nm region. Excluding the 91.2–117 nm contribution, the fluxes in the MAST website sum up to $\log L_{\rm EUV} = 27.39$. The close agreement of the EUV luminosity computed by these three different techniques (27.26, 27.38, and 27.39) provides confidence that all three techniques can provide realistic estimates of the unobservable EUV luminosity of M dwarf stars.

4. Spectral distribution of the total stellar flux

The synthetic spectrum of model 3346 in the top panel of Figure 9 has an integrated-average disk intensity of 1.96×10^4 erg s^{-1} cm^{-2} sr^{-1} over the 0.515–12.4 nm X-ray region, and the model's intensity in the X-ray band is slightly higher than the *ROSAT* measurement. The figure also compares the average disk intensity of model 3346 (GJ 832) to model 1401 (quiet Sun) and model 1404 (active Sun). We call attention to the increase in the emission with decreasing wavelength when comparing model 3346 to the solar models. At 200 nm the average disk intensity for model 3346 is nearly 4 orders of magnitude smaller than for the quiet Sun (model 1401), whereas in the EUV range (30–91.2 nm) the two models have comparable intensities. At shorter wavelengths ($\lambda < 40$ nm) model 3346 has larger intensities than model 1401. Thus the spectral energy distribution of GJ 832 is "hotter" than the quiet Sun and comparable to the active Sun at $\lambda < 91.2$ nm.

Table 2 compares the total flux of model 3346 to the quiet and active Sun models all evaluated at a distance of 1 AU. The table also compares the fraction of the model flux in different wavelength bands. The hotter spectral-energy distribution of GJ 832 is confirmed in this table by showing that in the 0.2–50 nm band, the fraction of GJ 832's flux is 30 times larger than the quiet Sun model and also larger than the active Sun model. For the FUV band, the fraction of the flux for GJ 832 is slightly larger than for the quiet Sun, but in the NUV band, the fraction of GJ 832's flux is 120 times smaller.

The middle of the habitable zone (HZ) for a hypothetical exoplanet of GJ 832 is 0.23 AU, the mean distance between the "runaway greenhouse" and "maximum greenhouse" limits described by Kopparapu et al. (2014). At this distance from its host star, the exoplanet would see fluxes $(0.23)^{-2} = 18.9$ times larger than is shown in Figure 9. As seen from their respective HZs, GJ 832 is much fainter than the quiet Sun in the 150–200 nm band, brighter in the 120–150 nm band, 30 times brighter than the quiet Sun

and comparable to the active Sun (model 1404) in the EUV and 50–120 nm bands, and brighter than the active Sun model at shorter wavelengths. The UVC band (100–280 nm) is important for biogenesis processes and DNA damage to life forms on planetary surfaces not protected by atmospheric absorption of UV radiation. Except for major flare events, the smaller radiation over most of the UVC band that is received at the surface of a hypothetical exoplanet in the HZ of GJ 832 compared to that seen at Earth from the present-day Sun could, therefore, place important constraints on the origin and evolution of possible life forms on such an exoplanet (e.g., Buccino et al. 2006, 2007).

The NUV flux of GJ 832 at 1 AU is smaller than solar, but is substantially larger than what would be expected from an M star without a chromosphere. This flux is due to the line emissions produced in the upper chromosphere of our model, where nonradiative heating takes place. The FUV line ratios indicate that the chromosphere-corona transition region of GJ 832 is more biased to hotter material than that of the quiet Sun. Also, the corona of GJ 832 appears to be hotter, but comparable to a substantially active Sun. From these trends and our models, we find that the EUV flux of GJ 832, which heats the outer atmospheres of exoplanets and drives their mass loss, is larger than that of the quiet Sun and comparable to a substantially active Sun.

5. DISCUSSION

5.1. Contribution Functions

We calculate contributions functions, i.e., attenuated emissivity, as defined by Equation 1 in Paper I. We show in Figure 10 the contribution functions for the line centers and peaks of the Ca II H and Mg II h lines as a function of pressure and corresponding temperature in model 3346. While the centers of these optically thick lines are formed at

relatively high temperatures, e.g., 10,000 to 20,000 K for Mg II, the line peaks are formed near 6000–7000 K and the line wings are formed at temperatures as low as 4000 K.

As shown in the left panel of Figure 11, the centers of the optically thick C II lines are formed near 25,000 K, but their line wings are also formed at much cooler temperatures. For the optically thin Si IV, C IV, and N V lines, there are no wings formed at cool temperatures. The temperature corresponding to the largest contribution to the line center emission increases from Mg I to N V, but the contribution functions for all of these species have tails extending to much higher temperatures, because above the temperature of peak ion abundance the increase in collisional excitation rates with temperature partially compensates for the decrease in ion abundance with temperature.

The broad temperature ranges over which the emission lines are formed requires that an acceptable atmospheric model must be able to fit many spectral lines formed over a wide temperature range at the same time. Models computed to fit only a limited set of chromospheric diagnostics (e.g., Hα and Ca II H and K lines) will not be representative of the entire atmosphere and may not even be an accurate model for the chromosphere as higher temperature plasma can contribute to the line center emission.

We used the contributions plots in Figures 10 and 11 to adjust and fine-tune model 3346 to match the observations. For example, reducing the spacing between the temperature-pressure grid points in the model where an emission line is formed decreases the total integrated intensity, while expanding the distance between points increases the intensity. This adjustment can be done locally with little effect on other nearby lines.

The different thermal structures for the GJ 832 and quiet Sun models are responsible for the different formation conditions of important ions and spectral lines. For example, unlike the Sun, the low temperatures in the upper photosphere and lower chromosphere of GJ 832 result in Ca being almost entirely neutral. As a result, the Ca II H and K lines are

formed only in a narrow region at higher temperatures in the upper chromosphere, and the line wings are narrower than in solar spectra. The Ca I absorption lines and TiO bands are much stronger in GJ 832 than in the Sun because of the cool photosphere. The Mg II h and k lines are also narrower than in the Sun, because Mg II is abundant where the temperature rises steeply in the upper chromosphere and the line cores are formed, but there is very little Mg II in the cool lower chromosphere where the broad wings are formed in the Sun. The Si IV, C IV, and N V lines are formed at 40,000–170,000 K in the transition region of the GJ 832 model, which is similar to their regions of formation in solar models.

5.2. Thermal Structure and Emission Line Strength

Vernazza, Avrett, & Loeser (1981) showed that the strong flux of chromospheric and transition region emission lines in the quiet-Sun network and plage regions can be explained by semi-empirical models in which the sharp temperature rise in the transition region occurs deeper in the atmosphere where the pressure and density are higher. This is confirmed and extended to active regions as shown by models in Fontenla, Avrett, & Loeser (2002) and Papers I–IV. If the temperature gradient in the transition region is the same, the effect of higher pressure at a given temperature is to increase the flux of optically thin lines such as C IV proportional $P_{\rm TR}^2$ and to increase the flux of optically thick lines such as Ca II H and K and Mg II h and k by a smaller amount. Grids of M-dwarf models built to fit the observed Ca II and H-α lines, including the models of Hawley & Fisher (1992) and Houdebine & Stempels (1997), also show that increasing Ca II flux and the transition of H-α from an absorption to an emission line naturally follow from thermal structures with increasing pressure in the upper chromosphere and transition region.

In our model 3346 for GJ 832, the transition region pressure is about 4 times larger than model 1401 for the quiet Sun (Figure 1), implying that the transition-region lines on

model 3346 should be 16 times brighter per unit area on the star. However, Table 1 shows that after correction for the factor of 4 smaller surface area of GJ 832 compared to the Sun, the surface fluxes of transition region lines are about the same in both models, because the transition region of GJ 832 has a much steeper temperature gradient that compensates for its higher pressure. The much cooler chromosphere of GJ 832 compared to the quiet Sun naturally explains why the relative emission of GJ 832 compared to the quiet Sun increases rapidly from the NUV to shorter wavelengths as shown in Section 4 and Figure 9.

In model 3346, the transition region occurs at a pressure $P_{\rm TR} = 0.8$ dynes cm^{-2}, which corresponds to a mass column density, $m = P_{\rm TR}/g$, $\log m = -4.8$ for the stellar gravity $\log g = 4.7$ (Schiavon, Barbuy, & Singh 1997). This value of $\log m$ is in the middle of the range for the grid of M1 dwarfs computed by Houdebine & Stempels (1997) and a factor of 2 smaller than for the quiet M-dwarf model (QT3) computed by Hawley & Fisher (1992).

5.3. Net Radiative-Loss Function

The net radiative-loss rate of a plasma at a given temperature (also called the total radiative-cooling loss) is an essential input for estimating the energy balance in a wide variety of astrophysical environments, including quasars, galactic clusters, interstellar medium, and stellar atmospheres. The ingredients needed for calculating the net radiative loss as a function of plasma temperature, which we call the net radiative loss function (NRLF), include the assumed abundances, ionization and recombination rates, excitation rates, the important continuum and line-emission processes, and a comprehensive catalog of oscillator strengths and collisional-excitation rates.

Early computations of the NRLF (e.g., Cox & Tucker 1971; McWhirter et al. 1975; Raymond, Cox & Smith 1976) included bremsstrahlung, recombination radiation, and

emission from a limited number of spectral lines, but these calculations assumed an optically thin plasma in all transitions and no molecules or dust. These functions showed peak emission at 1–3$\times10^5$ K with a steep dropoff at lower temperatures. Subsequent calculations for solar models (e.g., Avrett 1981) showed the importance of Ca II and Mg II in providing a peak in the NRLF at temperatures between 5,000 and 6,000 K. In their non-LTE calculations for a solar model that included a large number of spectral lines from neutral and singly ionized atoms, Anderson & Athay (1989) found that the Fe II lines contribute about half of the NRLF in the lower chromosphere. Using the Pandora code, Vieytes, Mauas, & Cincunegui (2005) and Vieytes et al. (2009) computed non-LTE models for G and K dwarf stars to fit the Ca II and Hβ lines, and computed NRLFs in the lower and upper chromospheres. The NRLF computed in Paper II for the quiet Sun is compatible with those computed by Anderson & Athay (1989), and the NRLFs for active regions on the Sun are substantially larger. Avrett et al. (2015) computed NRLFs for H I, Ca II, Mg II, and Fe II in their quiet-Sun and sunspot models, and Houdebine (2010b) computed NRLFs for two M dwarfs, GJ 867A and AU Mic (quiesecent and plage).

Figure 12 compares the NRLF for the GJ 832 model with those for a quiet Sun model (1401) and an active Sun model (1404). We assume that all spectral lines formed in the transition region and corona are optically thin, but for all other lines that may be optically thick we compute in non-LTE the NRLF for transitions between two atomic levels, also called the net radiative bracket. At temperatures above 100,000 K, the NRLFs of the two stars are the same, because the emission is from plasmas with the same abundances and all transitions are optically thin. Below 100,000 K, the functions differ because fitting the GJ 832 transition region line fluxes requires a much steeper thermal gradient in the the transition region than for the Sun, leading to increased thermal diffusion of neutral H upward into the transition region and, therefore, stronger Ly-α emission (cf. Fontenla, Avrett, & Loeser 2002). The thermal gradient in the GJ 832 model is sufficiently

steep that diffusion leads to H being 5% neutral at 66,000 K.

We also compare in Figure 12 our NRLF with that computed by McWhirter et al. (1975), which has often been used for studying the energy balence of hot astrophysical plasmas. The often used $T^{-1/2}$ fit to the McWhirter et al. (1975) NRLF shown in Figure 12 lies below the new function at $T > 20,000$ K, but has a similar slope at temperatures above 100,000 K. The new atomic data and many more lines of highly ionized Fe and other elements in the new models, and the diffusion of neutral H in the transition region, likely explain why the McWhirter et al. (1975) NRLF is low and should not be used at temperatures below 10^5 K, because it diverges substantially from the atmospheric models. The figure also shows the NRLF computed by Fontenla, Avrett, & Loeser (2002) based on older atomic rates and a high abundance of oxygen. The difference with the newer solar and GJ 832 models is mainly in the 20,000–100,000 K temperature range where some lines are optically thick and thermal diffusion of neutral hydrogen is important.

5.4. Problems fitting the Mg I 285.2 nm Emission Line

Our selection of the best temperature-pressure distribution in the chromosphere was driven by the need to fit the observed Ca II and Mg II lines. These lines are formed in an overlaping temperature range with the main contribution for the Ca II lines in the temperature plateau near 4500 K (left panel of Figure 10) and the Mg II lines at slightly higher temperatures (right panel of Figure 10). There is also a significant contribution to the formation of the Ca II lines at temperatures down to 4000 K where the Mg I 285.2 nm line is formed. We found that in order to fit both the Ca II and Mg II lines, we needed a chromospheric thermal structure that produces too much flux in the Mg I line. We have explored whether the overly bright Mg I emission could be reduced with different chromospheric thermal structures, Mg abundance, or continuum opacity without

a solution. We conclude that the bright Mg I line likely results from inaccuracies in the atomic ionization and recombination rates. Our model uses an approximate formula for these rates, but Osorio et al. (2015) have recently computed new rates for inelastic electron and hydrogen atom collisional ionization of Mg I including charge transfer. Unfortunately, they do not publish rates for Mg I ionization or recombination, and in the application of the Mg I rates to a grid of non-LTE model atmospheres (Osorio & Barklem 2016) does not include these rates.

5.5. The effect of different thermal structures in M dwarf and solar models on the formation of the Ly-α line and electron densities

The cooler upper chromosphere of GJ 832 does not contribute as much to the Ly-α flux as the warmer upper chromosphere in solar models. For GJ 832 the line is formed almost entirely in the transition region through the particle diffusion process that allows neutral H to exist at relatively high temperatures. This process also dominates the emission in the solar Ly-α line center, but the peaks and wings of the solar line are formed mainly in the upper chromosphere, which is not the case for GJ832 because of the cooler temperatures in its upper chromosphere.

Another important difference between GJ 832 and the Sun is that the electron density in the cooler chromosphere of GJ832 is much smaller than in the solar chromosphere. In the solar chromosphere, the heavy species are singly ionized everywhere, but in GJ 832 they are mostly neutral in the lower chromosphere and then become singly ionized in the upper chromosphere due to the temperature increase and density decrease with height. Thus, processes such as the Farley-Buneman instability can only occur in the lower chromosphere of GJ 832 at low densities where the residual electrons that have a density of $\sim$ 2–3$\times10^9$ cm^{-3} can be heated to collisionally ionize the heavy abundant elements (Mg, Si, Fe),

increasing the electron density to $\sim 10^{10}$ cm^{-3}. In the case of the quiet Sun, the electron density never decreases below $\sim 5 \times 10^{10}$ cm^{-3} and rises to about $\sim 10^{11}$ cm^{-3} in the upper chromosphere. While the electron densities in GJ 832's chromosphere are about ten times smaller than in the Sun, the higher pressure in GJ 832's lower transition region results in higher electron densities comparable to moderately active solar regions.

6. SUMMARY AND CONCLUSIONS

This paper describes a complete physical model and synthetic spectrum for the M-dwarf star GJ 832 computed to fit the observed UV and optical spectra and the X-ray flux. This is the first semi-empirical model of an M star including the photosphere, chromosphere, transition region, and corona that is computed in full non-LTE using the Solar-Stellar Radiation Modeling tools previously employed for computing the most recent comprehensive solar-atmosphere models. The GJ 832 model can serve as a prototype for computing an exoplanet's complete radiation environment, in particular the unobservable EUV flux, when observations are not available because of the absence of suitable telescopes (especially *HST*) or our inability to observe a host star at earlier times in its evolution. We compute very high-resolution synthetic spectra ($\lambda/\Delta\lambda \sim 10^6$) from X-rays to the infrared for comparison with important diagnostics including the emission lines of Ca II, Mg II, Lyα, Hα C II-IV, Si III-IV, and N V. We list here our results and conclusions:

(1) Our model 3346 for GJ 832 differs quantitatively from the quiet Sun model 1401, but has qualitative similarities. The photosphere and lower chromosphere of the GJ 832 model are much cooler than the quiet Sun model at the same pressures with a minimum temperature of about 2600 K compared to about 3800 K for the quiet Sun. However, the pressure corresponding to the minimum temperature is not very different for both models. Above the temperature minimum, both models have a steep temperature rise to a somewhat

curved "plateau" near 4700 K for GJ 832 and 6300 K for the quiet Sun.

(2) The spectral energy distribution of GJ 832 is "hotter" than for the quiet Sun. Comparing the average disk intensity of GJ 832 (model 3346) to the quiet Sun (model 1401), we find that GJ 832 is nearly 10^4 times fainter at 200 nm, but comparable to the quiet Sun in the 91–130 nm spectral region and much brighter than the quiet Sun in the X-ray and EUV bands (0–91 nm). The excellent agreement of our computed EUV luminosity with that obtained by two other techniques indicates that our model predicts reliable EUV emission from GJ 832.

(3) Compared to the Sun, GJ 832 may be slightly metal deficient, but probably not as metal deficient as log[Fe/H]=–0.12 proposed by Johnson & Apps (2009). The fit to the TiO fluxes assuming solar abundances is consistent with metal abundances being close to solar.

(4) We compute the temperature dependence of the net radiative-loss function (NRLF) for model 3346 using modern atomic oscillator strengths and collisional rates, non-LTE radiative transfer, and a thermal structure for an M dwarf that provides the basis for computing future theoretical atmospheric models based on energy balance and heating rates. At temperatures above 100,000 K, the NRLF for GJ 832 is the same as for quiet and active solar models, because the abundances are the same in these models and all transitions are optically thin. The much steeper temperature gradient in the transition region of GJ 832 results in strong diffusion of neutral H into the transition region and a much larger NRLF at 20,000–100,000 K than for the quiet Sun.

While model 3346 does an excellent job of fitting the observed UV and optical emission lines and continua, our approach to semi-empirical modelling indicates the need for future work. The computed Mg I 285.2 nm shows the photospheric absorption more or less correctly but has a large central emission that is only very weak in the observed profile. We believe that this discrepancy is the result of incorrect atomic ionization/recombination

rates that allow too much Mg I to be present in the upper chromophere. Although small changes in the chromospheric thermal structure between 4000 and 5000 K may also be significant, our tests showed that with the current ionization/recombination rates such changes would lead to too large Mg II emissions before the Mg I emission becomes small. The larger width of the shoulders of the computed Lyman-α emission line could result from the approximations used in the PRD or from inaccurate atomic collisional and ionization data for the C I continua that overlap the Lyman-α wings. We find that the inclusion of molecular absorption lines (especially TiO but also other diatomics) is essential for fitting the wings of the Na I D and Hα lines. Finally, we suggest that the opacity sources in the NUV, and particularly the H_2, need further study.

While our semi-empirical model for GJ 832 incorporates state-of-the-art radiative transfer techniques and atomic and molecular rates, it does not attempt to describe atmospheric inhomogeneity or time variability. If the Sun is a useful guide, then M dwarfs should have three-dimensional structures, active regions, starspots, flares, and other forms of spatial and temporal variability. Such phenomena are indeed observed. Inclusion of these effects will challenge future modelers, but the present model should be a useful basis for understanding the mean radiative output of M-dwarf stars that is of great interest for studying the habitability of exoplanets. We look forward to a new generation of models for stars cooler than the Sun that will guide our understanding of stellar phenomena and physical processes and the radiation environment of their exoplanets.

7. ACKNOWLEDGMENTS

This work is supported by grants HST-GO-13650 and HST-GO-12464 from the Space Telescope Science Institute to the University of Colorado. We appreciate the availability of the *HST* data through the MAST Web site hosted by the Space Telescope Science Institute,

and stellar data through the SIMBAD database operated at CDS, Strasbourg, France. The authors thank the diligent referee for his many helpful suggestions, Dr. Reiner Hammer, Dr. Svetlana Berdyugina, and Dr. Alexander Brown for their helpful comments, and Dr. Allison Youngblood for advice on the EUV flux and computing the reconstructed Ly-α flux. Finally, JLL thanks the Kiepenheuer Institut für Sonnenphysik for hospitality and an opportunity for shared insights.

Facilities: HST (COS), HST (STIS), CXO (ASIS).

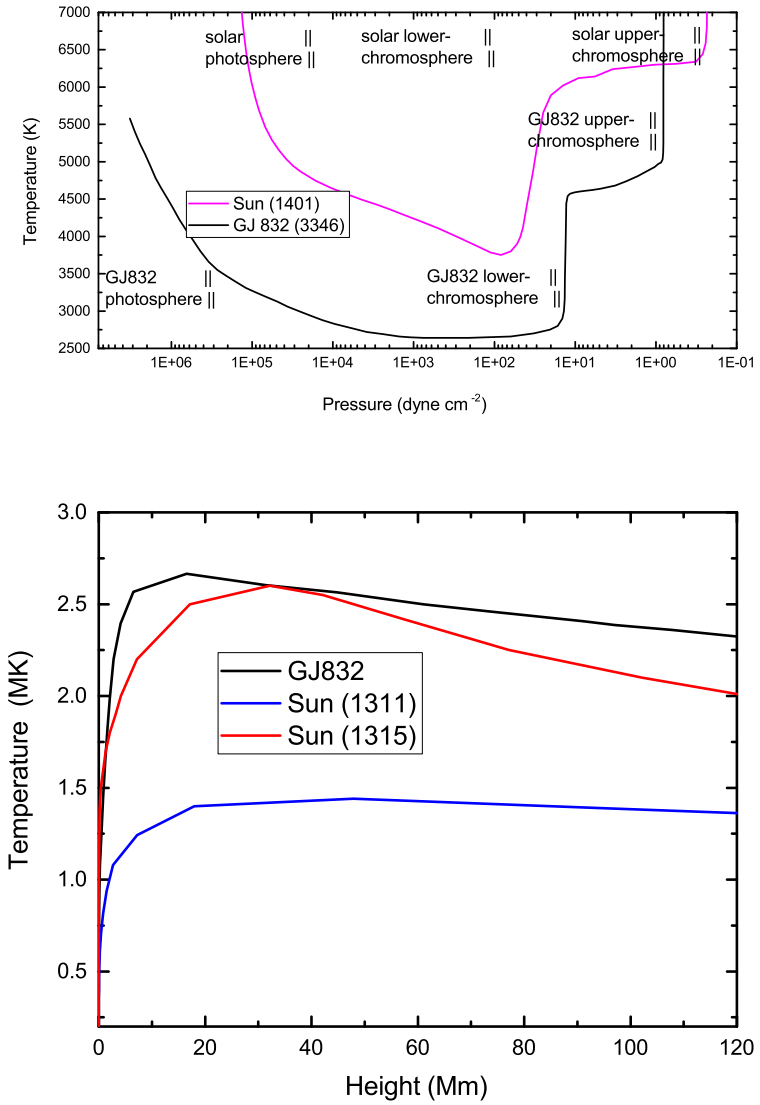

Fig. 1.— *Top panel:* Temperature versus gas pressure distributions for GJ 832 (model 3346, red line) and the quiet-Sun inter-network model 1401 (purple line) from Paper V. The double vertical lines designate boundaries: the solar and GJ 832 photospheres occur at higher pressures to the left of the left-most sets of double lines, the lower chromospheres lie between the first and second sets of double lines, and the upper chromospheres lie between the second and third sets of double lines. The temperature minima of the models are at $P \approx 100$ dynes cm^{-2}, and the steeply rising temperature in the transition region and extended coronal layers (not shown) lie above the upper chromosphere. *Bottom panel:* Temperature versus height for the GJ832 model 3346 (black line) compared with the quiet-Sun inter-network model 1311 (blue) and the very bright solar plage model 1315 (red) from Paper IV.

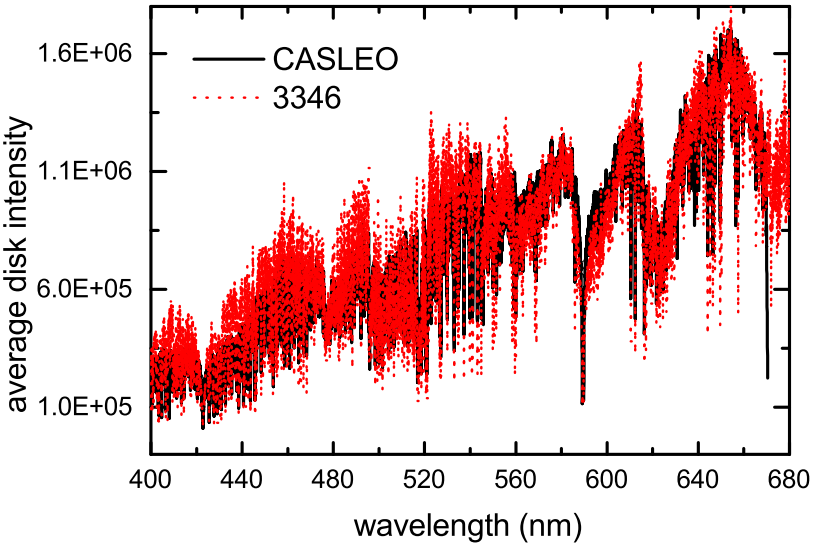

Fig. 2.— The average disk intensity (erg s^{-1} cm^{-2} nm^{-1} sr^{-1}) of GJ 832 in the optical region observed by CASLEO on Sep 2012 (black) is compared with the computed spectrum from our model 3346 (red).

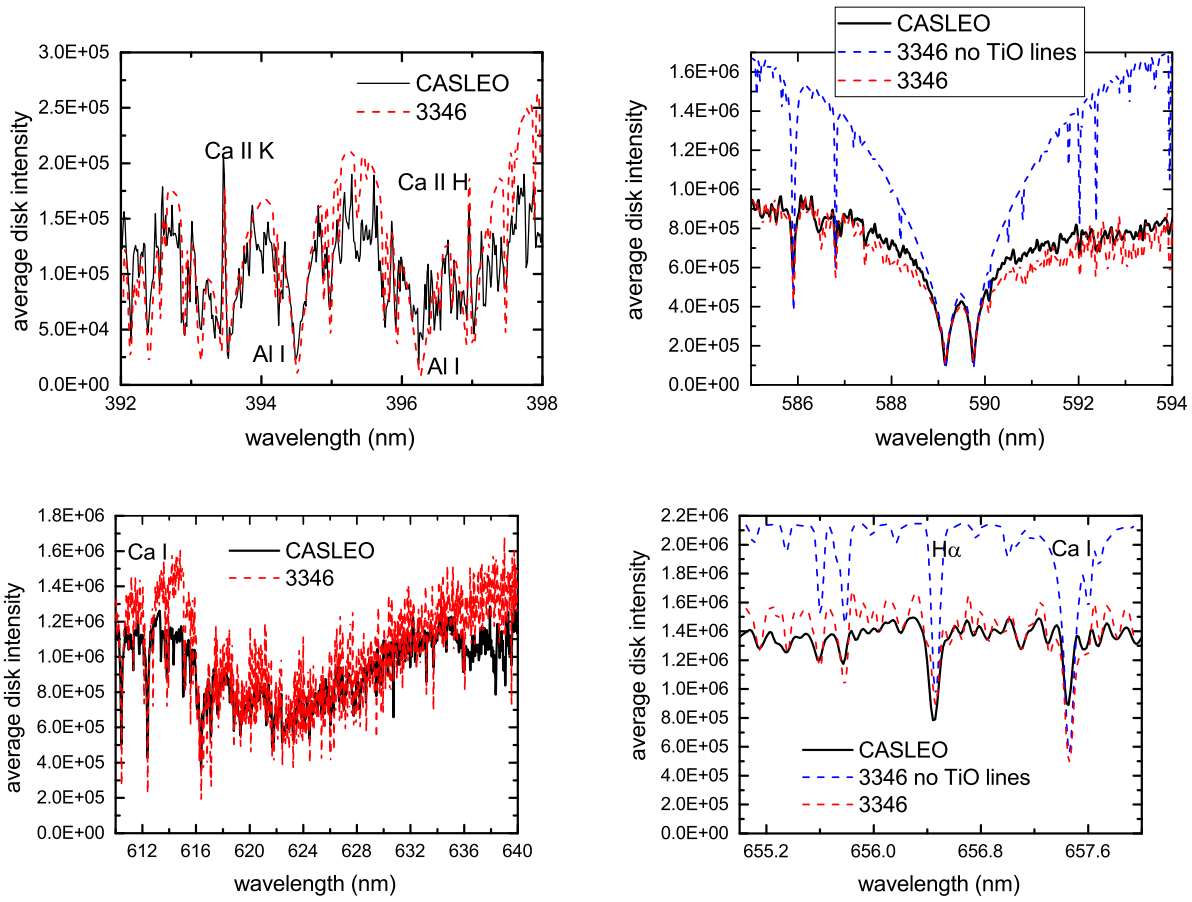

Fig. 3.— Comparison of the average disk intensity (erg s^{-1} cm^{-2} nm^{-1} sr^{-1}) of GJ 832 observed at CASLEO (black lines) with the computed spectrum of model 3346 (red lines). *Upper left panel:* Ca II H and K spectral region; *upper right panel:* Na I D lines region; *lower left panel:* one of the TiO bands; *lower right panel:* Hα region. The Ca II H emission line is located just below the H symbol in the upper left panel. The blue lines in the upper right and lower right panels show the effect of not including TiO line absorption.

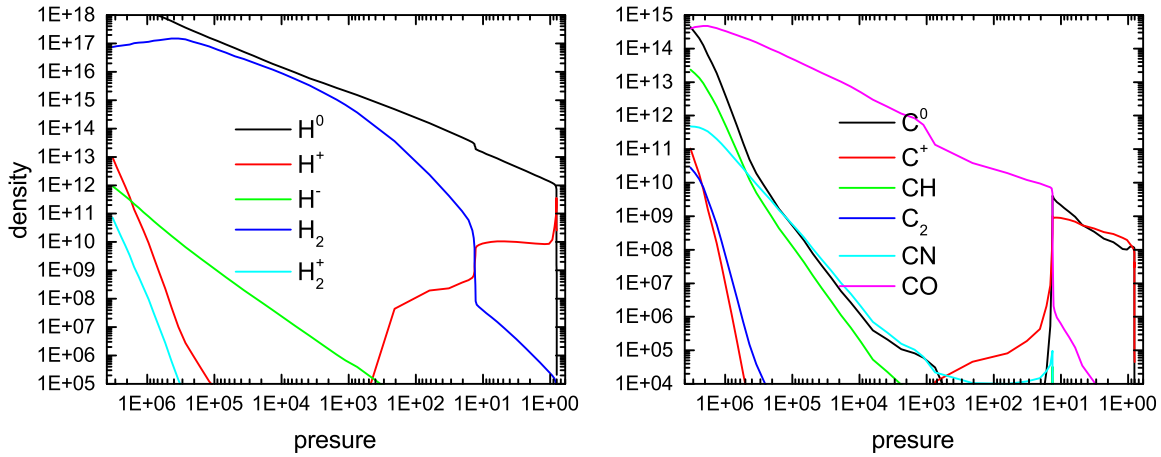

Fig. 4.— Computed densities for H (*left panel*) and C (*right panel*) in atomic, ionic, and molecular forms. In the photosphere, H_2 is as abundant as atomic H, and CO is the dominant form of carbon below the upper chromosphere. In the upper chromosphere where the temperature rises steeply at $P \approx 1$ dyne cm^{-2}, singly ionized H and C both become the dominant species.

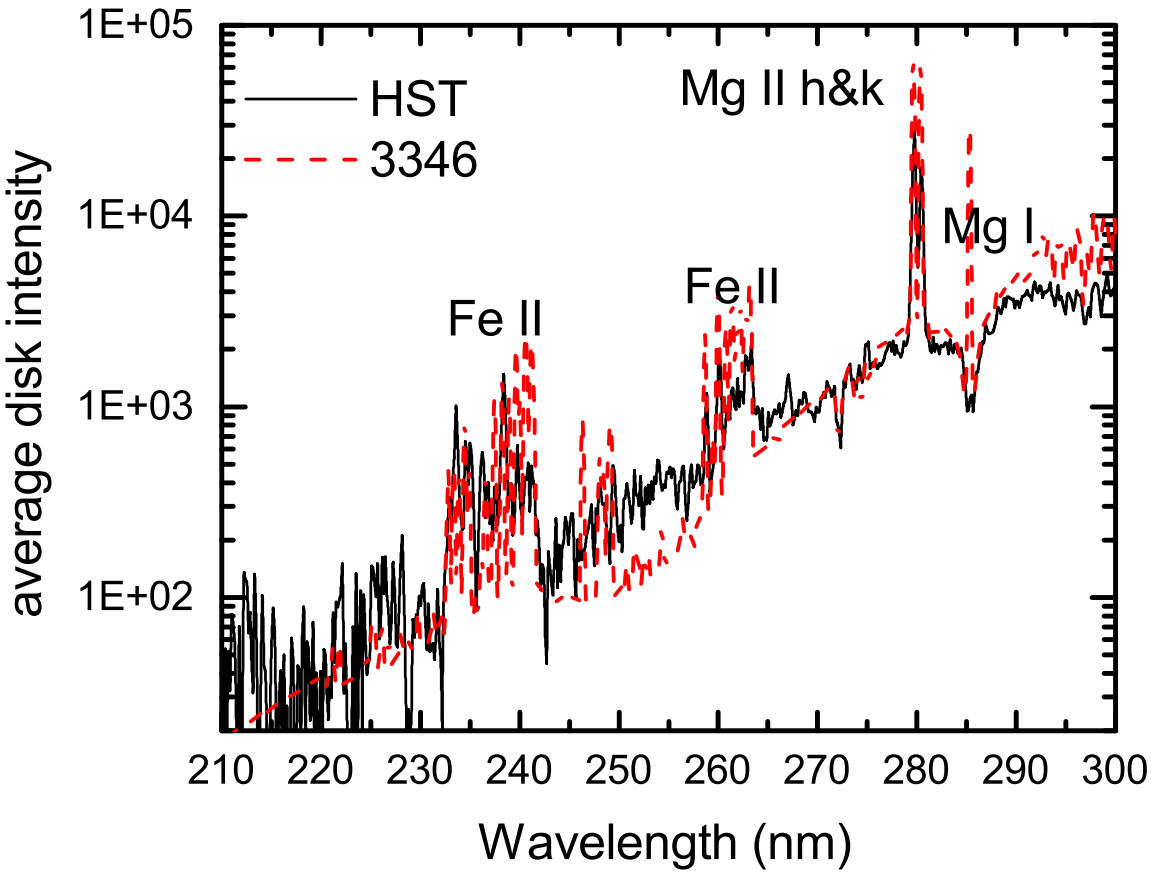

Fig. 5.— Model 3346 (red line) and observed *HST* (black line) NUV spectra of GJ 832 average disk intensity. Prominent spectral features are marked.

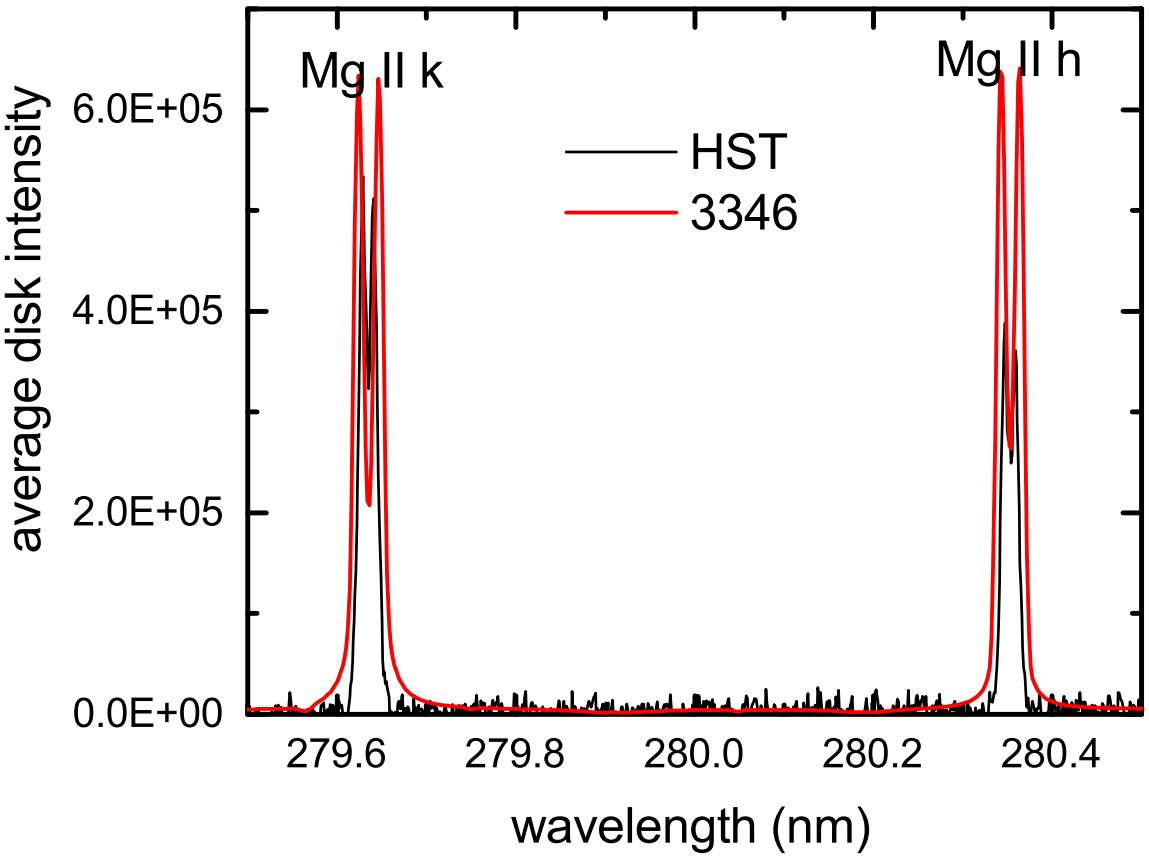

Fig. 6.— Comparison of high-resolution intensity (erg cm^{-2} s^{-1} Å^{-1} sr^{-1}) of the Mg II h (280.3 nm) and k (279.6 nm) lines of GJ 832 computed from model 3346 (red line) and observed (black line) with *HST*. The computed Mg II line profiles do not include interstellar absorption (see Section 3.3).

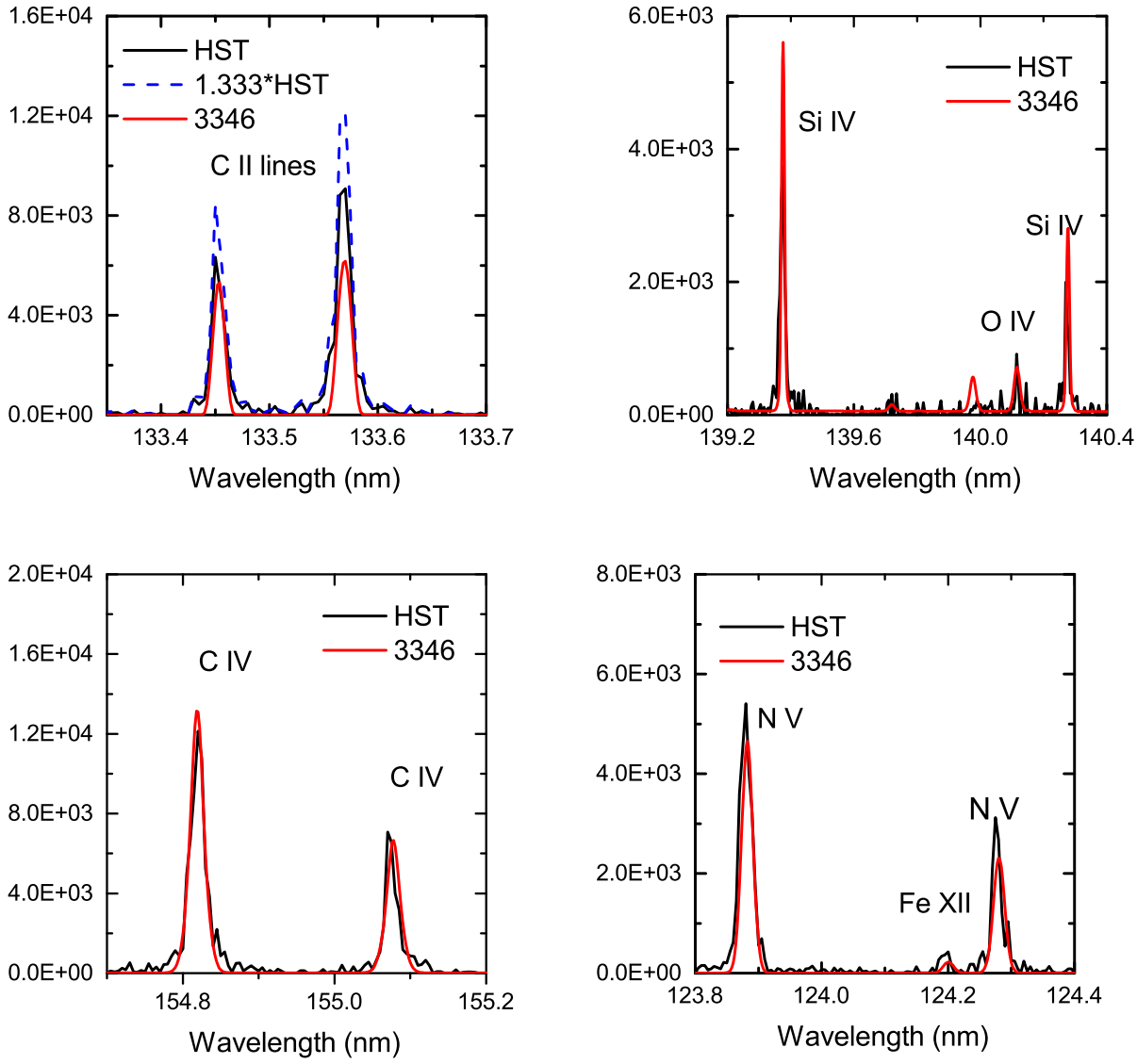

Fig. 7.— Comparison of model 3346 average disk intensity UV line profiles (red lines) with GJ 832 line profiles (black lines) observed by *HST*. *Upper left:* C II line centers are formed near $T = 25,000$ K. The dashed blue line shows the 30% correction to the observed intensity for interstellar absorption. *Upper right:* Si IV lines are formed near 50,000 K and O IV lines are formed near 160,000 K; *Lower left:* C IV lines are formed near 100,000 K; and *Lower right:* N V lines are formed near 170,000 K and the Fe XII line is formed near 1.4×10^6 K.

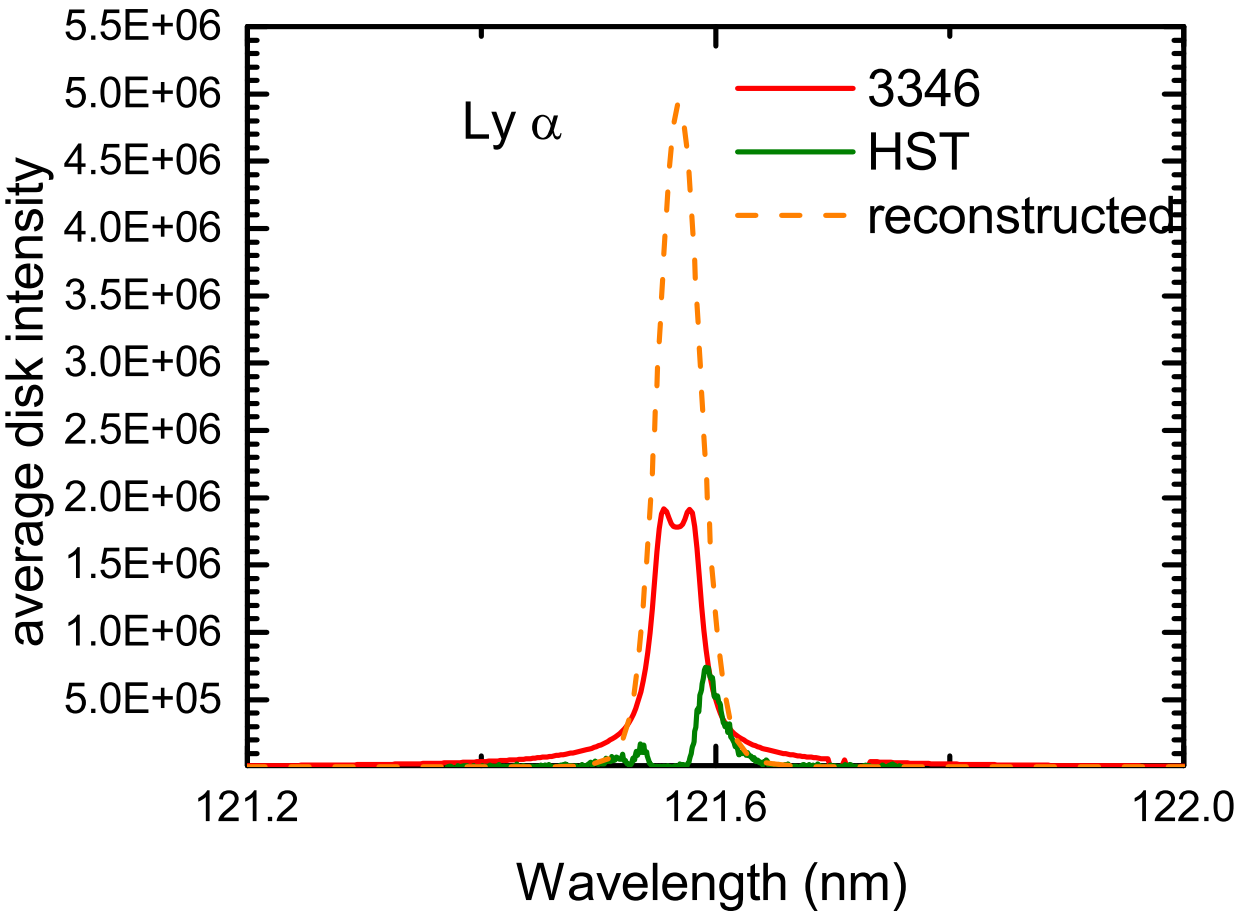

Fig. 8.— Comparison of the GJ 832 Ly-α emission line observed by *HST* (green line) with the model 3346 average disk intensity (red line) and the observed Ly-α line (orange dashed line) reconstructed to remove interstellar absorption.

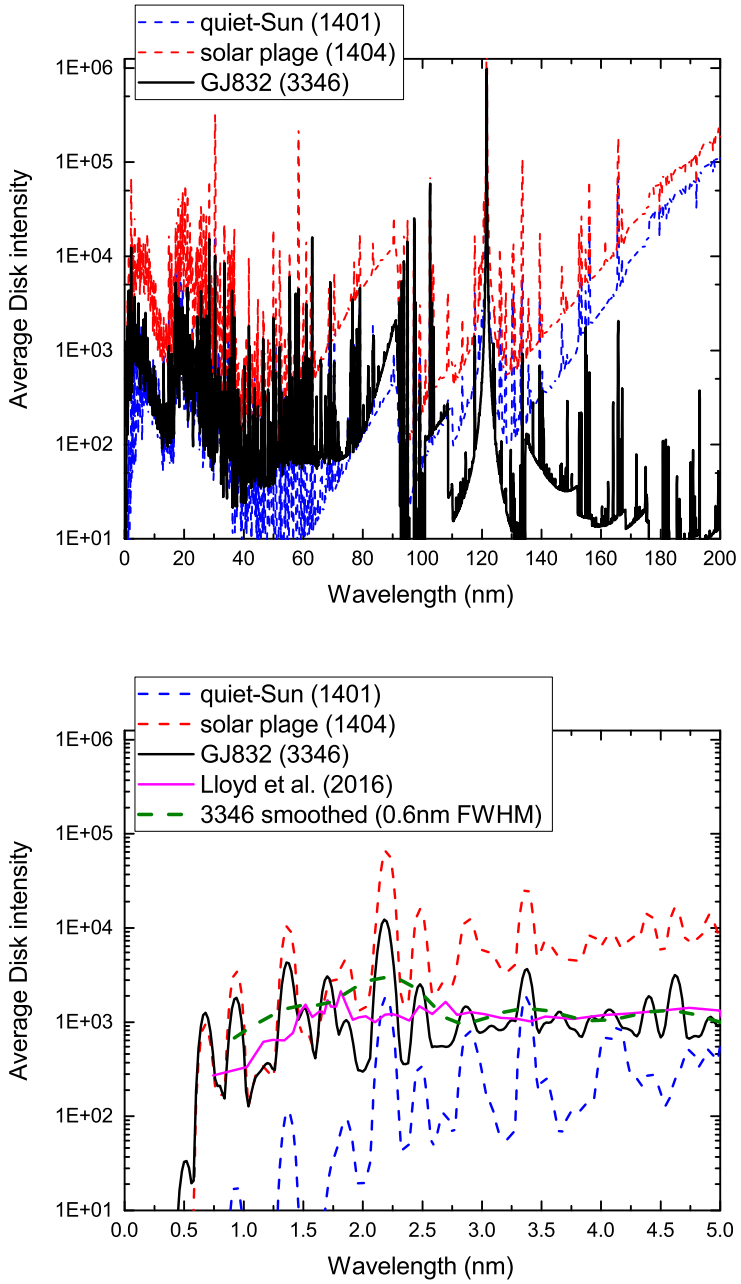

Fig. 9.— *Top panel:* The spectral synthesis spectrum of GJ 832 (model 3346, black line) convolved with a 0.1 nm FWHM $\cos^2$ filter. Units of the average disk intensity are erg s^{-1} cm^{-2} nm^{-1} sr^{-1}. For comparison, we show spectra of the quiet Sun (model 1401, blue line) and active Sun (model 1404, red line). The brightest emission lines are H I Lyman-α λ121.567 nm and He II Lyman-α λ30.391 nm. *Bottom panel:* An expanded plot showing the observed XMM spectrum of GJ 832 (pink solid line) and model spectra for GJ 832 (black line), the quiet Sun (dashed blue line), and a solar plage (dashed red line). The dashed green

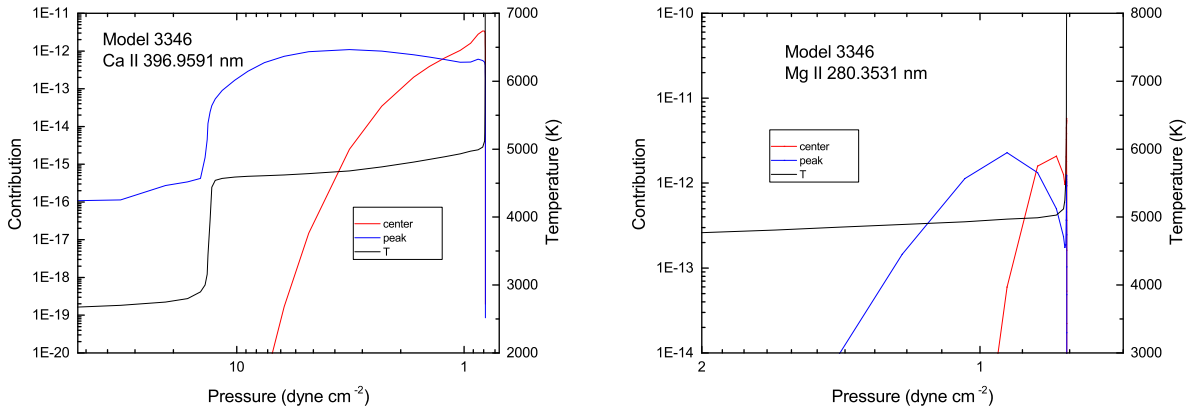

Fig. 10.— *Left panel:* Contribution function (attenuated emissivity) at line center (red line) and emission peaks (blue line) for the Ca II H and K lines. *Right panel:* Same for the Mg II h and k lines. Also plotted is the temperature vs. pressure (black line).

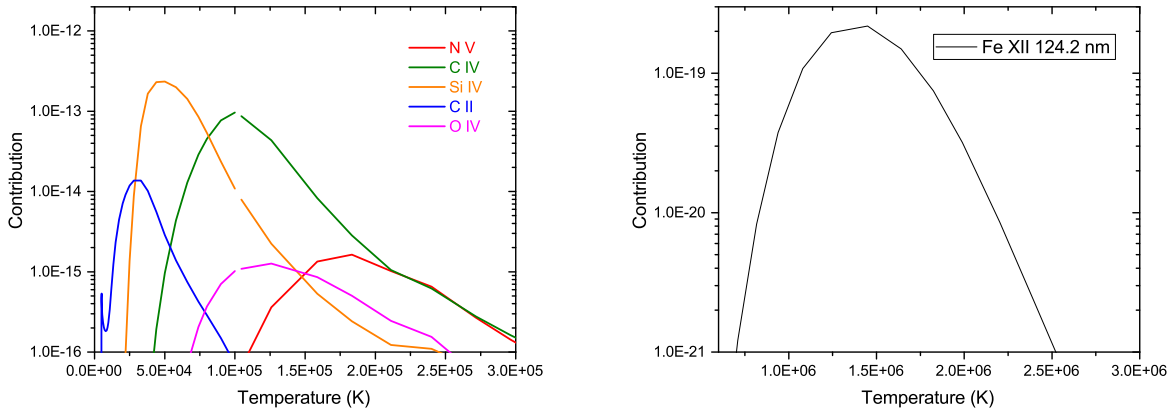

Fig. 11.— *Left panel:* Contribution functions for transition region lines. *Right panel:* Contribution function for the Fe XII 124.200 nm line.

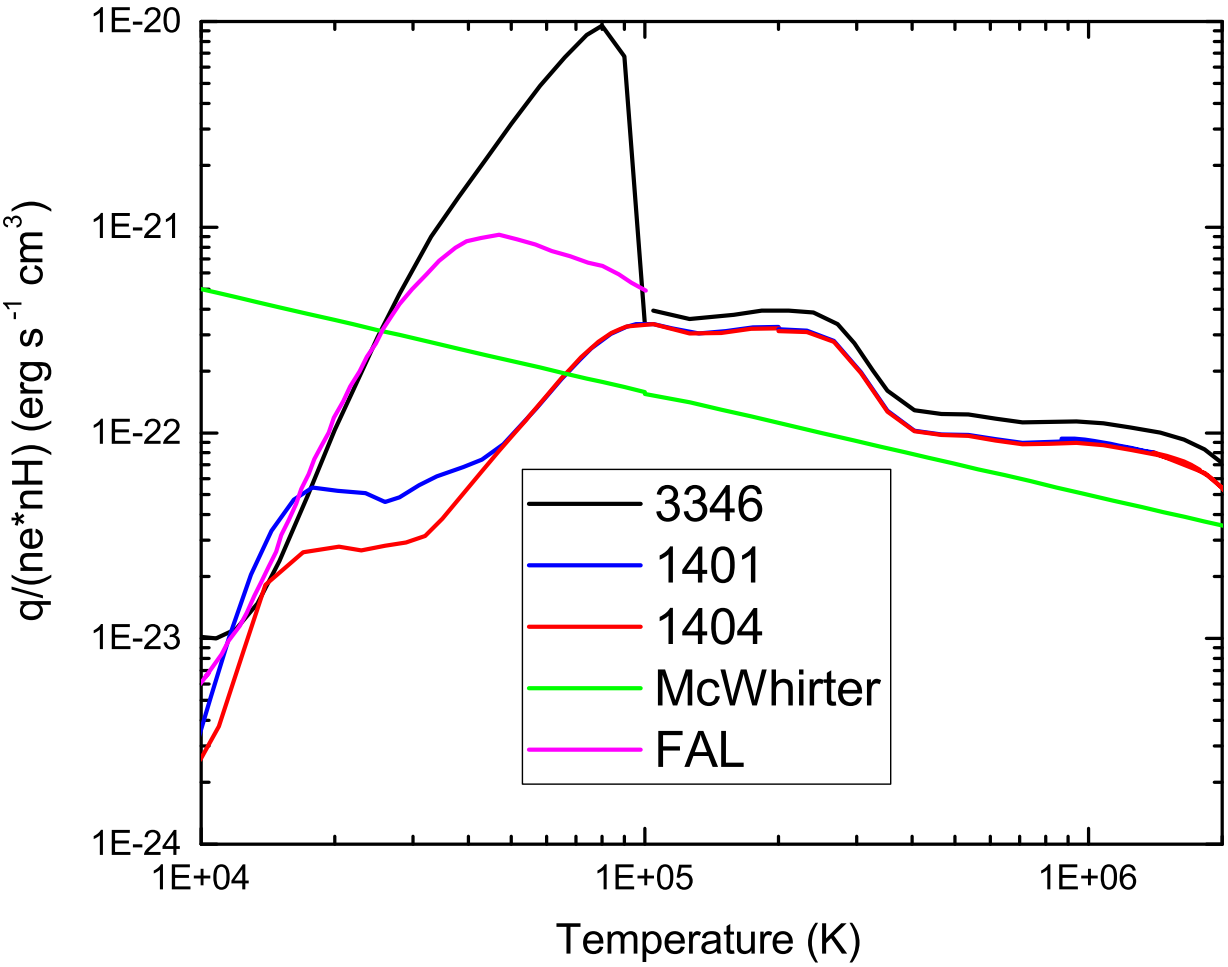

Fig. 12.— Comparison of the net radiative-loss function (NRLF) for GJ832 (model 3346, black) with corresponding functions for the quiet Sun (1401, blue) and active Sun (1404, red). For temperatures above 100,000 K, the NRLFs in the transition region and corona are the same for both stars. Below 100,000 K, the NRLFs differ because the steep thermal gradient in the transition region of model 3346 induces strong diffusion of neutral H to high temperatures where Ly-α is an efficient radiator. Also shown is the NRLF (pink) for a solar model computed by Fontenla, Avrett, & Loeser (2002) and a fit (green) to the NRLF computed by McWhirter et al. (1975)

.

REFERENCES

Aurière, M. 1982, A&A, 109, 301

Allard, F. & Hauschildt, P. H. 1995, ApJ, 445

Allard, F. et al. 2010, ApJ, 540, 1005

Allard F., Hauschildt P. H., Alexander D. R., Tamani A., & Schweitzer A. 2001, ApJ, 556, 357

Anderson, L. S. & Athay, R. G. 1989, ApJ, 346, 1010

Avrett, E. H. 1981, in Solar Phenomena in Stars and Stellar Systems, ed. R.M. Bonnet & A.K. Dupree, (Dordrecht: D. Reidel Publishing Co.), p. 173

Avrett, E. H. and Loeser, R. 2008, ApJS, 175, 229

Avrett, E., Tian, H., Landi, E., Curdt, W., & Wülser 2015, ApJ, 811, 87

Baglin, A. 2003, Ad. Space Res., 31, 345

Bailey, J., Butler, R. P., Tinney, C. G., et al. 2009, ApJ, 690, 743

Batalha, N. M., Rowe, J. F., Bryson, S. T. et al. 2013, ApJS, 204, 24

Berger, E., Basri, G., Giampapa, M. S. et al. 2010, ApJ, 709, 332

Bessell, M. S. PASP, 107, 672

Blandford, R. D., Haynes, M. P., Hucra, J. P. 2010, New Worlds, New Horizons in Astronomy and Astrophysics, (Washington, D.C.: National Academies Press)

Bonfils, X., Delfosse, X., Udry, S., Santos, N. C., Forveille, T., Ségransan, D., 2005, A&A, 442, 635

Bonfils, X., Delfosse, X., Udry, S., et al. 2013, A&A, 549, A109

Bozhinova, I., Helling, C., & Scholz, A. 2015, MNRAS, 450, 160

Brain, D., Barabash, S., Boesswetter, A., et al. 2010, Icarus, 206, 139

Buccino, A. P., Lemarchand, G. A., & Mauas, P. J. D. 2006, Icarus, 183, 491

Buccino, A. P., Lemarchand, G. A., & Mauas, P. J. D. 2007, Icarus, 192, 582

Buccino, A. P., Díaz, R. F., Luoni, M. L., Abrevaya, X. C., & Mauas, P. J. D., 2011, AJ, 141, 34

Buccino, A. P., Petrucci, R., Jofré, E., & Mauas, P. J. D. 2014, ApJ,781, 9

Burton, W. M., Ridgeley, A., & Wilson, R. 1967, MNRAS, 135, 207

Cincunegui, C. & Mauas, P. J. D. 2004, A&A, 414, 699

Chadney, J. M., Galand, M., Unruh, Y. C., Koskinen, T. T., & Sanz-Forcada, J. 2015, Icarus, 250, 357

Cox, D. P. & Tucker, W. H. 1971, ApJ, 157, 1157

Cram, L. E. & Giampapa, M. S. 1987, ApJ, 323, 316

Des Marais, D. J., Harwit, M. O., Jucks, K. W., Kasting, K. W., Lin, D. N. C., Lunine, J. I., Schneider, J., Seager, S., Traub, W. A., & Wolfe, N. J. 2002, AsBio, 2, 153

Doyle, J. G., Mathioudakis, M., Andretta, V., Short, C. I., & Jelinsky, P. 1997, A&A, 318, 835

Dressing, C. D., & Charbonneau, D. 2015, ApJ, 807, 45

Engle, S. G., Guinan, E. F., & Mizusawa, T. 2009, AIP Conf. Proc., 1135, 221

Evans, D. S., Menzies, A., Stoy, R. H., & Wayman, P. A. 1961, Royal Obs. Bull., 48

Fontenla, J., White, O. R., Fox, P. A., Avrett, E. H., & Kurucz, R. L. 1999, ApJ, 518, 480

Fontenla, J. M., Avrett, E. H., & Loeser, R. 2002, ApJ, 572, 636

Fontenla, J., Balasubramaniam, K. S., & Harder, J. 2007, ApJ, 667, 1243 (Paper I)

Fontenla, J, M., Curdt, W., Haberreiter, M., Harder, J., & Tian, H. 2009, ApJ, 707, 482 (Paper II)

Fontenla, J. M., Harder, J., Livingston, W., Snow, M., & Woods, T. 2011, J. Geophys. Res., 116, D20108 (Paper III)

Fontenla, J. M., Landim E., Snow, M., & Woods, T. 2014, Sol. Phys., 289, 515 (Paper IV)

Fontenla, J. M., Stancil, P. C., & Landi, E. 2015, ApJ, 809, 157 (Paper V)

Fleming, T. A., Schmitt, J. H. M. M., & Giampapa, M. S. 1995, ApJ, 450, 401

France, K., Linsky, J. L., Tian, F., Froning, C. S., & Roberge, A. 2012, ApJ, 750, L32

France, K., Froning, C. S., Linsky, J. L., Roberge, A., Stocke, J. T., Tian, F., Bushinsky, R., Désert, J.-M., Mauas, P., Vieytes, M., & Walkowicz, L. M. 2013, ApJ, 763, 149

France, K., Loyd, R. O. P., Youngblood, A. et al. 2016, ApJ, 820, 89

Fuhrmeister, B., Schmitt, J. H. M. M., & Hauschildt, P. H. 2005, A&A, 439, 1137

Gomes da Silva, J., Santos, N. C., Bonfils, X., Delfosse, X., Forveille, T., Udry, S., Dumusque, X., & Lovis, C. 2012, A&A, 541, 9

Gustafsson, B., Edvardsson, B., Eriksson, K., Jorgensen, U. G., Nordlund, A. A., & Plez, B. 2008, A&A, 486, 951.

Hauschildt, P. H. & Baron, E. 2008, A&A, 490, 873

Hawley, S. L. & Fisher, G. H. 1992, ApJS, 78, 565

Houdebine, E. R. 2009, MNRAS, 397, 2133

Houdebine, E. R. 2010a, A&A, 509, A65

Houdebine, E. H. 2010b, MNRAS, 403, 2157

Houdebine, E. H. 2010c, A&A, 509, 65

Houdebine, E. R., Mathioudakis, M., Doyle, J. G., & Foing, B. H. 1996, A&A, 305, 209

Houdebine, E. R., & Stempels, H. C. 1997, A&A, 326, 1143

Johnson, J. A. 2014, Phys. Today, 67, issue 10, p. 11

Johnson, J. A. & Apps, K. 2009, ApJ, 699, 933

Jordan, C., McMurry, A. D., Sim, S. A., & Arulvel, M. 2001, MNRAS, 322, L5

Kashyap, V. L., Drake, J. J., & Saar, S. H. 2008, ApJ, 687, 1339

Kasting, J. F., Whitmire, D. P. & Reynolds, R. T. 1993, Icarus, 101, 108

Koch, D. G., Borucki, W. J., Basri, G., et al. 2010, ApJ, 713, L79

Kopparapu, R. K., Ramirez, R., Kasting, J. F. et al. 2013, ApJ, 765, 131

Kopparapu, R. K., Ramirez, R. M., SchottelKotte,J., et al. 2014, ApJ, 787, L29

Landi, E., Young, P. R., Dere, K. P., Del Zanna, G., & Mason, H. E. 2013, ApJ, 763, 86

Lanza, A. F. 2008, A&A, 486, 1163

Linsky, J. L., France, K., & Ayres, T. 2013, ApJ, 766, 69

Linsky, J. L., Fontenla, J., & France, K. 2014, ApJ, 780, 61

Llama, J. & Shkolnik, E. L. 2015, ApJ, 802, 41

Loyd, R. O. P., France, K., Youngblood, A. et al. 2016, ApJ, 824, 102

Maldonado, J., Affer, L., Micela, G. et al. 2015, A&A, 577, A132

Martens, P. C. H. 2010, ApJ, 714, 1290

Mauas, P. J. D. 2000, ApJ, 539, 858

Mauas, P. J. D., Falchi, A., Pasquini, L., & Pallavicini, R. 1997, A&A, 326, 249

McWhirter, R. W. P., Thonemann, P. C., & Wilson, R. 1975, A&A, 40, 63

Miguel, Y., Kaltenegger, L., Linsky, J. L., & Rugheimer, S. 2015, MNRAS, 446, 345

Mihalas, D. 1978, Stellar Atmospheres Second Edition, (San Francisco: W.H. Freeman & Co.)

Murray-Clay, R. A., Chiang, E. I. & Murray, N. 2009, ApJ, 693, 23

Newton, E. R., Irwin, J., Charbonneau, D., Berta-Thompson, Z. K., & Dittmann, J. A. 2016, ApJ, 821, L19

Newton, E. R., Irwin, J., Charbonneau, D., Berta-Thompson, Z. K., Dittmann, J. A., & West, A. A. 2016, ApJ, 821, 93

Osorio,Y. & Barklem, P. S. 2016, A&A, 586, A120

Osorio, Y., Barklem, P. S., Lind, K., Belyaev, A. K., Spielfiedel, A., Guitou, M., & Feautrier, N. 2015, A&A, 579, 530

Pagano, I., Linsky, J. L., Carkner, L., Robinson, R. D., Woodgate, B., & Timothy, G. 2000, ApJ, 532, 497

Pagano, I., Linsky, J. L., Valenti, J., & Duncan, D. K. 2004, A&A, 415, 331

Pérez, M. I. P., Schröder, K.-P., & Hauschildt, P. 2014, MNRAS, 445, 270

Plez, B. 1998, A&A, 337, 495

Poppenhaeger, K., Robrade, J., & Schmitt, J. H. M. M. 2010, A&A, 515, A98

Poppenhaeger, K. & Wolk, S. J. 2014, A&A, 565, 1

Raymond, J. C., Cox, D. P., & Smith, B. W. 1976, ApJ, 204, 290

Redfield, S. & Linsky, J. L. 2008, ApJ, 673, 283

Robinson, R. D., Cram, L. E., & Giampapa, M. S. 1990, ApJS, 74, 891

Robrade, J., & Schmitt, J. H. M. M. 2005, A&A, 435, 1073

Rosner, R., Tucker, W. H., & Viana, G. S. 1978, ApJ, 220, 643

Sanz-Forcada, J., Ribas, I., Micela, G., Pollock, A. M. T., Garca-Álvarez, D., Solano, E., & Eiroa, C. 2010, A&A, 511, A8

Sanz-Forcada, J., Micela, G., Ribas, I., Pollock, A. M. T., Eiroa, C., Velasco, A., Solano, E., & Garca-Álvarez, D. 2011 A&A, 532, A6

Scalo, J., Kaltenegger, L., Segura, A., et al. 2007, AsBio, 7, 85

Schiavon, R. P., Barbuy, B., & Singh, P. D. 1997, ApJ, 484, 499

Schmitt, J. H. M. M., Fleming, T. A., & Giampapa, M. S 1995, ApJ, 450.392

Seager, S., Deming, D., & Valenti, J. A. 2009, in Astrophysics in the Next Decade, Astrophysics and Space Science Proceedings (Netherlands: Springer), p. 123

Segura, A., Walkowicz, L. M., Meadows, V., Kasting, J., & Hawley, S. 2010, AsBio, 10, 751

Shkolnik, E., Walker, G. A. H., & Bohlender, D. A. 2003, ApJ, 597, 1092

Shkolnik, E., Walker, G. A. H., Bohlender, D. A., Gu, P.-G., & Kürster, M. 2005, ApJ, 622, 1075

Short, C. I. & Doyle, J. G. 1998, A&A, 336, 613

Stauffer, J. R., & Hartmann, L. W. 1986, Cool Stars, Stellar Systems and the Sun, in Lecture Notes in Physica 254 (Berlin: Springer), 58

Stelzer, B., Marino, A., Micela, G., López-Santiago, J., & Liefke, C. 2013, MNRAS, 431, 2063

Suárez Mascareño, A., Rebolo, R., González Hernández, J. I., & Esposito, M. 2015, MNRAS, 452, 2745

Tarter, J. C., Backus, P., Mancinelli, R. L. et al. 2007, Astrobiology, 7, 30

Tian, F., Kasting, J. F., Liu, H., & Roble, R. G. 2008, J. Geophys. Res., 113, 5008

Tian, F., France, K., Linsky, J. L., Mauas, P. J. D., & Vieytes, M. C. 2014, Earth Planet. Sci. Lett., 385, 22

van Leeuwen, F. 2007, A&A, 474, 653

Vernazza, J. E., Avrett, E. H., & Loeser, R. 1981, ApJS, 45, 635

Vieytes, M. C., Mauas, P. J. D., & Cincunegui, C. 2005, MNRAS, 398, 1495

Vieytes, M. C., Mauas, P. J. D., Díaz, R. F. 2009, MNRAS, 398, 1495

Walkowicz, L. M. & Hawley, S. L. 2009, AJ, 137, 3297

Wedemeyer, S., Ludwig, H.-G., & Steiner, O. 2013, AN, 334, 137

West, A. A., Weisenburger, K. L., Irwin, J., Berta-Thompson, Z. K., Charbonneau, D., Dittmann, J. & Pineda, J. S. 2015, ApJ, 812, 3

Wittenmyer, R. A., Tuomi, M., Butler, R. P. et al. 2014, ApJ, 791, 114

Wood, B. E., Müller, H.-R., Zank, G. P., Linsky, J. L., & Redfield, S. 2005, ApJ, 628, L143

Youngblood, A., France, K., Loyd, R. O. P. 2016, ApJ, 824, 101

This manuscript was prepared with the AAS LaTeX macros v5.2.

Table 1. Fluxes[a] (erg cm^{-2} s^{-1} at 1 AU) of observed and computed emission lines

Line and wavelength (nm)	GJ 832 MUSCLES	GJ 832 Model 3346	quiet Sun Model 1401	active Sun Model 1405
Ly-α 121-122	3.86[b]	2.13	2.44	46.1
Mg II k 279.6352	0.192[c]	0.321	30.9	114
Mg II h 280.3531	0.129[c]	0.309	29.2	106.7
Ca II K 393.4777	0.196[d]	0.163[e]	–	–
Ca II H 396.9591	0.159[d]	0.157[e]	–	–
C II 133.5708	2.47e-3[c]	2.60e-3	5.52e-2	4.01
C II 133.4532	1.74e-3[c]	1.18e-3	5.19e-2	4.01
Si IV 139.3757	1.46e-3	1.33e-3	2.81e-3	0.266
Si IV 140.2772	6.44e-4	6.95e-4	1.42e-2	0.113
C IV 154.8189	5.28e-3	5.17e-3	2.86e-2	0.147
C IV 155.0775	2.47e-3	2.60e-3	1.79e-2	9.18e-2
O IV 140.1158	1.74e-4	2.69e-4	4.62e-3	2.42e-2
N V 123.8823	2.26e-3	1.74e-3	7.14e-3	3.89e-2
N V 124.2806	1.01e-3	8.66e-4	2.88e-3	2.10e-2
Fe XII 124.20	<1.07e-4	7.11e-5	5.23e-4	1.12e-2

[a]Conversion of intensity to flux at 1 AU assumes $R = 0.499 R_\odot$ for GJ 832. The angular diameter of GJ 832 at 1 AU is 1.691×10^{-5} sr. The angular diameter of the Sun at 1 AU is 6.7993×10^{-5} sr.

[b]Reconstructed Ly-α line flux from A. Youngblood (private communication). The

reconstructed Ly-α flux obtained by France et al. (2013) from the analysis of the same observed data is 5.21 erg cm^{-2} s^{-1} at 1 AU.

[c]Intrinsic stellar flux assuming 30% absorption by interstellar Mg II and C II.

[d]CASLEO flux measured with a rectangular extraction slit 0.10097 nm wide for the K line and 0.1274 nm wide for the H line.

[e]Flux computed from the model 3346 synthetic spectrum using a rectangular extraction slit 0.1170 nm wide for the K line and 0.1096 nm wide for the H line.

Table 2. Stellar surface radiative flux

	Total flux at 1AU	Short wave	FUV	NUV	Vis/NIR	FIR
	0.1 nm – 100 μm	0.2–50 nm	50–200 nm	200–400 nm	400 nm – 1.6 μm	1.6–100 μm
Units	erg cm^{-2} s^{-1}	relative[a]	relative[a]	relative[a]	relative[a]	relative[a]
GJ 832[b]	4.922e4	1.02e-5	5.85e-5	2.26e-3	0.642	0.356
quiet Sun	1.388e6	1.12e-6	8.30e-5	0.087	0.803	0.110
active Sun	1.437e6	2.46e-5	2.67e-4	0.098	0.794	0.108

[a]Fraction of total flux in this wavelength interval, relative to the flux reported in column 1.

[b]Model 3346.